



AFRL-AFOSR-VA-TR-2022-0047

**Understanding Superacid Interaction on Semiconductor/Oxide Interfaces for
Mobility Enhancement in THz Applications**

**Zeng, Yuping
UNIVERSITY OF DELAWARE
220 HULLIHEN HALL
NEWARK, DE, 19716
USA**

**09/09/2021
Final Technical Report**

DISTRIBUTION A: Distribution approved for public release.

Air Force Research Laboratory
Air Force Office of Scientific Research
Arlington, Virginia 22203
Air Force Materiel Command

REPORT DOCUMENTATION PAGE

Form Approved
OMB No. 0704-0188

The public reporting burden for this collection of information is estimated to average 1 hour per response, including the time for reviewing instructions, searching existing data sources, gathering and maintaining the data needed, and completing and reviewing the collection of information. Send comments regarding this burden estimate or any other aspect of this collection of information, including suggestions for reducing the burden, to Department of Defense, Washington Headquarters Services, Directorate for Information Operations and Reports (0704-0188), 1215 Jefferson Davis Highway, Suite 1204, Arlington, VA 22202-4302. Respondents should be aware that notwithstanding any other provision of law, no person shall be subject to any penalty for failing to comply with a collection of information if it does not display a currently valid OMB control number.
PLEASE DO NOT RETURN YOUR FORM TO THE ABOVE ADDRESS.

1. REPORT DATE (DD-MM-YYYY) 09-09-2021	2. REPORT TYPE Final	3. DATES COVERED (From - To) 01 Jun 2019 - 31 May 2021
--	--------------------------------	--

4. TITLE AND SUBTITLE Understanding Superacid Interaction on Semiconductor/Oxide Interfaces for Mobility Enhancement in THz Applications	5a. CONTRACT NUMBER
	5b. GRANT NUMBER FA9550-19-1-0297
	5c. PROGRAM ELEMENT NUMBER 61102F

6. AUTHOR(S) Yuping Zeng	5d. PROJECT NUMBER
	5e. TASK NUMBER
	5f. WORK UNIT NUMBER

7. PERFORMING ORGANIZATION NAME(S) AND ADDRESS(ES) UNIVERSITY OF DELAWARE 220 HULLIHEN HALL NEWARK, DE 19716 USA	8. PERFORMING ORGANIZATION REPORT NUMBER
---	---

9. SPONSORING/MONITORING AGENCY NAME(S) AND ADDRESS(ES) AF Office of Scientific Research 875 N. Randolph St. Room 3112 Arlington, VA 22203	10. SPONSOR/MONITOR'S ACRONYM(S) AFRL/AFOSR RTA1
	11. SPONSOR/MONITOR'S REPORT NUMBER(S) AFRL-AFOSR-VA-TR-2022-0047

12. DISTRIBUTION/AVAILABILITY STATEMENT
A Distribution Unlimited: PB Public Release

13. SUPPLEMENTARY NOTES

14. ABSTRACT
The goal of this project is to understand the Superacid (TFSI) Interactions on Semiconductor/Oxide Interfaces for Mobility Enhancement in THz Applications. We have successfully implemented the superacid treatment methods and applied them on different materials and devices including InAs fin field effect transistors, TiO2 thin film transistors, InAs/MoS2 heterojunction as well as MoS2 metal oxide semiconductor field effect transistors, GaN high electron mobility transistors. We have studied the interactions between superacid and MoS2/ZrO2, between superacid and InAs/ZrO2 interface, between superacid and InAs/MoS2 interface, between superacid and TiO2/ZrO2, between superacid and GaN/ZrO2. We applied material characterization techniques (X-ray Photoelectron spectroscopy, Raman spectroscopy, Photoluminescence spectroscopy, etc) to evaluate material and interface properties. We performed C~V and I~V characterizations to examine the electrical properties after interactions with SA. It is found that superacid plays a key role in enhancing the performances of these devices including MoS2, InAs, TiO2 transistors. (1) For MoS2 transistors, TFSI treatment can effectively improve the electron mobility and gate controllability of ML MoS2 transistors; (2) For InAs transistors, the interfacial oxide at the InAs/ZrO2 interface was effectively reduced after TFSI treatment due to strong protonating nature of SA solution; (3) For TiO2 transistors, SA treatment was found to enhance the on-current by nearly 2x; (4) For GaN transistors, SA treatment was found to slightly enhance the GaN transistors performance; (5) For InAs/MoS2 interface, the rectifying ratio of the pn junction between InAs/MoS2 is enhanced by superacid treatment. Our future work will be developing the superacid treatment process and incorporate the method into various transistors technology for THz applications.

15. SUBJECT TERMS

16. SECURITY CLASSIFICATION OF:			17. LIMITATION OF ABSTRACT	18. NUMBER OF PAGES	19a. NAME OF RESPONSIBLE PERSON KENNETH GORETTA
a. REPORT	b. ABSTRACT	c. THIS PAGE			19b. TELEPHONE NUMBER (Include area code)
U	U	U	UU	49	426-7349

Understanding the Superacid Interactions on Semiconductor/Oxide Interfaces for Mobility Enhancement in THz Applications

Program manager: Kenneth Goretta Funding number: FA9550-19-1-0297

final report: 06/01/2019-5/31/2021

PI: Yuping Zeng yzeng@udel.edu

Department of Electrical and Computer Engineering

University of Delaware

(Students involved in this work: Guangyang Lin, Jie Zhang, Peng Cui, Kazy Shariar, Qi Cheng, Lincheng Wei)

Abstract

The goal of this project is to understand the Superacid (TFSI) Interactions on Semiconductor/Oxide Interfaces for Mobility Enhancement in THz Applications.

We have successfully implemented the superacid treatment methods and applied them on different materials and devices including InAs fin field effect transistors, TiO₂ thin film transistors, InAs/MoS₂ heterojunction as well as MoS₂ metal oxide semiconductor field effect transistors, GaN high electron mobility transistors. We have studied the interactions between superacid and MoS₂/ZrO₂, between superacid and InAs/ZrO₂ interface, between superacid and InAs/MoS₂ interface, between superacid and TiO₂/ZrO₂, between superacid and GaN/ZrO₂. We applied material characterization techniques (X-ray Photoelectron Spectroscopy, Raman spectroscopy, Photoluminescence spectroscopy, etc) to evaluate material and interface properties. We performed C~V and I~V characterizations to examine the electrical properties after interactions with SA.

It is found that superacid plays a key role in enhancing the performances of these devices including MoS₂, InAs, TiO₂ transistors. (1) For MoS₂ transistors, TFSI treatment can effectively improve the electron mobility and gate controllability of ML MoS₂ transistors; (2) For InAs transistors, the interfacial oxide at the InAs/ZrO₂ interface was effectively reduced after TFSI treatment due to strong protonating nature of SA solution; (3) For TiO₂ transistors, SA treatment was found to enhance the on-current by nearly 2x; (4) For GaN transistors, SA treatment was found to slightly enhance the GaN transistors performance; (5) For InAs/MoS₂ interface, the rectifying ratio of the pn junction between InAs/MoS₂ is enhanced by superacid

treatment.

Our future work will be developing the superacid treatment process and incorporate the method into various transistors technology for THz applications.

Related Publications

The related results have been published in the following **12** journal papers and **2** conference paper and there is **one** manuscript is pending. We have also one preliminary patent filed on the GaN high electron mobility transistors.

Patent:

Peng Cui, Yuping Zeng, “A Two-Step Annealing on InAlN/GaN Source/Drain Contacts”, 2021. (U.S. Patent Application Serial No.: 63/208,529).

Journal papers

1. Peng Cui, Tzu-Yi Yang, Jie Zhang, Yu-Lun Chueh and Yuping Zeng, “Improved On/off current ratio and linearity of InAlN/GaN HEMTs with N₂O surface treatment for radio frequency application,” ECS Journal of solid state science and technology, No.10, 065013, 2021.
2. Peng Cui, Yuping Zeng, “Electrical properties of 90-nm InAlN/GaN HEMT on silicon substrate,” Physica E: Low-dimensional systems and nanostructures, Vol. 134, 114821, 2021.
3. Jie Zhang, Graduate Student Member, Yuying Zhang, Peng Cui, Guangyang Lin, Chaoying Ni, and Yuping Zeng, “One-Volt TiO₂ Thin Film Transistors With Low-Temperature Process,” IEEE Electron Device Letters, Vol. 42, No.4, pp.521-524, 2021.
4. Peng Cui, Meng Jia, Hang Chen, Guangyang Lin, Jie Zhang, Lars Gundlach, John Q Xiao, Yuping Zeng, “InAlN/GaN HEMT on Si with f_{max}= 270 GHz,” IEEE Transaction on Electron Devices, Vol. 68, No. 3, pp. 994-999, 2021.
5. Guangyang Lin, Haiyang Hong, Jie Zhang, Yuying Zhang, Peng Cui, Jianyuan Wang, Songyan Chen, Yong Zhao, Chaoying Ni, Cheng Li, Yuping Zeng, “Fabrication of SiGe/Ge nanostructures by three-dimensional Ge condensation of sputtered SiGe on SiO₂/Si substrate,” Journal of Alloys and Compounds, Vol.858, pp. 157653, 2020.
6. Peng Cui, Guangyang Lin, Jie Zhang, Yuping Zeng, “Sub-60 mV/decade Switching via Hot Electron Transfer in Nanoscale GaN HEMTs,” IEEE Electron Device Letters, Vol.40, No.8,

pp.1185-1188, 2020.

7. G. Lin, M. Zhao, M. Jia, P. Cui, H. Zhao, J. Zhang, L. Gundlach, X. Liu, A. C. Johnson, and Y. Zeng, "Improving the electrical performance of monolayer top-gated MoS₂ transistors by post bis (trifluoromethane) sulfonamide treatment," *Journal of Physics D: Applied Physics*, Vol. 53, pp.415106, 2020.
8. Guangyang Lin, Dongxue Liang, Zhiwei Huang, Chunyu Yu, Peng Cui, Jie Zhang, Jianyuan Wang, Jianfang Xu, Songyan Chen, Cheng Li, Yuping Zeng, "Fabrication of polycrystalline SiGe- and Ge-on-insulator by Ge condensation of amorphous SiGe on SiO₂/Si substrate," *Journal of Semiconductor Science and Technology*, 35, 095016, 2020.
9. Jie Zhang, Guangyang Lin, Peng Cui, Meng Jia, Zhengxin Li, Lars Gundlach, Yuping Zeng, "Enhancement-/Depletion-Mode TiO₂ Thin-Film Transistors via O₂/N₂ Pre-annealing," *IEEE Transactions on Electron Devices*, Volume 67, Issue 6, pp. 2346 -2351, 2020.
10. Guangyang Lin, Meng-Qiang Zhao, Meng Jia, Jie Zhang, Peng Cui, Lincheng Wei, Haochen Zhao, A. T. Charlie Johnson, Lars Gundlach and Yuping Zeng, "Performance enhancement of monolayer MoS₂ transistors by atomic layer deposition of high-k dielectric assisted by Al₂O₃ seed layer", *Journal of Physics D: Applied Physics*, Vol.53, 105103, 2019.
11. Kazy F Shariar, Guangyang Lin, Zijian Wang, Peng Cui, Jie Zhang, Robert Opila, Yuping Zeng, "Effect of Bistrifluoromethane sulfonimide treatment on Nickel/InAs contacts," *Applied Physics A*, 125, 429, 2019.
12. Yuping Zeng, Sourabh Khandelwal, Kazy Shariar, Zijian Wang, Guangyang Lin, Qi Cheng, Peng Cui, Robert Opila, Ganesh Balakrishnan, Sakhvikas Addamane, Peyman Taheri, Daisuke Kiriya, Mark Hettick, Ali Javey, "InAs FinFETs performance enhancement by superacid surface treatment," *IEEE Transaction on Electron Devices*, pp.1856-1861, Vol. 66, No. 4, April, 2019.

Conference papers

13. Peng Cui, Yuping Zeng, "HZO/InAlN/GaN MIS-HEMT on Silicon with SS of 60 mV/dec and f_T/f_{max} of 115/200 GHz", *Device Research Conference*, June, 2021.
14. Jie Zhang, Meng Jia, Guangyang Lin, Peng Cui and Yuping Zeng, "Ionic doping of TiO₂ thin film transistors using superacid treatment," *62nd Electronic Materials Conference*, June 24-26, 2020.

Pending

15. Guangyang Lin, Meng-Qiang Zhao, Peng Cui, Jie Zhang, Sadhvikas Addamane, Ganesh Balakrishnan, Ali Javey, A. T. Charlie Johnson and Yuping Zeng, "Gate tunable rectifying ratio between 2D MoS₂ and 3D InAs N-n type van der Waals heterojunction," under review, 2021.

Results

We will describe its effect in the following three aspects: (1) Superacid effectively improved the electrical performance of ML top-gated MoS₂ transistors; (2) Superacid plays an important role on enhancing InAs device performance; (3) Superacid plays an important role on enhancing the performance of TiO₂ thin film transistors; (4) For GaN transistors, SA treatment was found to slightly enhance the GaN transistors performance; (5) For InAs/MoS₂ interface, the rectifying ratio of the pn junction between InAs/MoS₂ is enhanced by superacid treatment.

1. Improving the electrical performance of ML top-gated MoS₂ transistors by post TFSI treatment

Bis(trifluoromethane) sulfonamide (TFSI) is a strong protonating agent with a large Hammett number (larger than sulfuric acid) [1]. The TFSI-treated molybdenum disulfide (MoS₂) has shown dramatic enhancement of photoluminescence (PL) intensity (quantum efficiency) [2-4]. However, the influence of TFSI treatment on the electrical performance of MoS₂ requires further investigation. At this point, we fabricated top-gated monolayer (ML) MoS₂ transistors and carried out post TFSI treatment. The electrical performance of ML MoS₂ transistors before and after TFSI treatment was systematically studied. It is found that TFSI treatment can effectively improve the electron mobility and gate controllability of ML MoS₂ transistors. Detailed mechanisms were analyzed by transmission line measurement (TLM), Raman spectra and X-ray photoelectron spectra (XPS).

Due to large surface to volume ratio of two-dimensional (2D) materials, the electrical performance of MoS₂ is very sensitive to extrinsic ambient conditions. Post treatments are favorable to improve or recover the electrical performance of MoS₂. Herein, the influence of post forming gas annealing (FGA) and bis(trifluoromethane) sulfonamide (TFSI) treatment on the electrical performance of monolayer (ML) top-gated MoS₂ transistors is investigated. The

results are analyzed by linear transmission-line-model (TLM) structure, Raman and XPS techniques. It is found that both FGA and TFSI treatment can effectively improve the electron mobility of MoS₂ due to desorption of water. However, FGA would result in deterioration of gate controllability due to introduction of S vacancies, while TFSI treatment can effectively improve the gate controllability. The results indicate that the electrical performance of MoS₂ and/or other S-containing 2D transition metal dichalcogenides (TMDs) can be effectively improved by post TFSI treatment.

1.1 Fabrication of ML top-gated MoS₂ transistors and post treatments

Monolayer MoS₂ flakes were grown by chemical vapor deposition (CVD) on a 300-nm SiO₂/Si substrate [5]. 30 nm Ti/50 nm Au was deposited on MoS₂ to form source (*S*) and drain (*D*) contacts. Samples were then baked at 120°C under vacuum for 12 h to remove moisture and adsorbate on MoS₂. Next, samples were immediately loaded into an e-beam evaporation chamber to evaporate 1 nm Al₂O₃ as seed layer for dielectric deposition on ML MoS₂. After that, a ~20-nm HfO₂ layer was grown on sample surface by atomic layer deposition (ALD). Ultimately, 30-nm Ti/50-nm Au was selectively deposited as the top gate (*G*) metal. The ML top-gated MoS₂ transistors were then subjected to FGA and TFSI treatments, respectively. The FGA was performed at 200°C for 30 min in forming gas composed of 95% N₂ and 5% H₂ by rapid thermal annealing (RTA), while a 0.2 mg/ml TFSI solution diluted in 1, 2-dichlorobenzene (DCB) was used for TFSI treatment [4]. The TFSI treatment was carried out in a tightly closed vial for 2 min on a 100°C hotplate. The chip was directly blown-dried by N₂ after TFSI treatment.

1.2 Electrical performance of ML top-gated MoS₂ transistors after FGA and TFSI treatment

Figure 1(a) compares the typical transfer curves ($I_{ds} \sim V_{gs}$) of the ML top-gated MoS₂ transistors before (black scatter) and after FGA (green scatter) under $V_{ds}=0.5$ V. After FGA, the V_{th} of ML MoS₂ transistor shifts negatively from -0.9 to -1.0 V. The μ_{eff} of ML MoS₂ has improved from 1.29 to 2.11 cm²·V⁻¹·s⁻¹. However, the on/off current ratio has decreased from >10⁷ to ~10⁶ and the minimum *SS* has deteriorated from 220 to 399 mV/dec. Figure 1(b) shows the statics figure

of SS ratio between the transistors after and before FGA along with a Gaussian simulation curve (red). The peak value of the SS ratio is around 1.5 verifying that the gate controllability of ML MoS₂ device is deteriorated after FGA. Figure 1(c) gives the static figure of μ_{eff} ratio between transistors after and before FGA along with corresponding Gaussian simulation curve (red). The peak value of the μ_{eff} ratio is around 1.6 corroborating that the μ_{eff} of ML MoS₂ is effectively improved after FGA. Figure 2(d) shows the output curves ($I_{ds} \sim V_{ds}$) for as-fabricated transistor (black curves) and transistor after FGA (green curves). Under $V_{gs} - V_{th} \approx 2$ V, the I_{ds} at $V_{ds} = 1$ V has increased from ~ 20 to ~ 37.5 μ A. The results indicate that the device resistance is reduced after FGA.

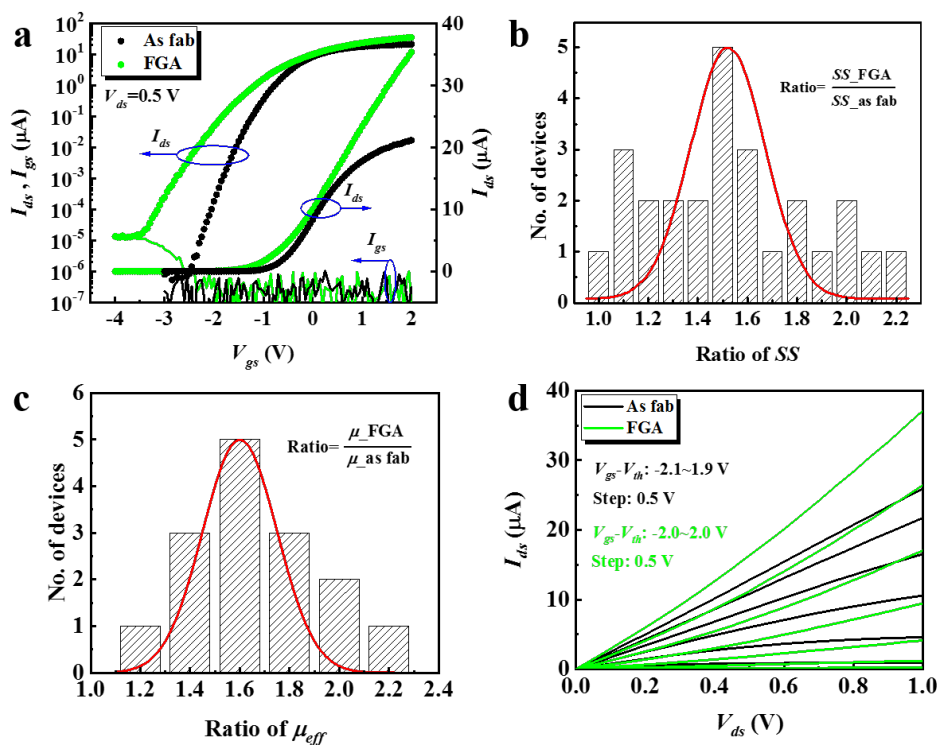


Fig. 1. (a) Comparison of transfer curves for ML top-gated MoS₂ transistor before (black scatter) and after FGA (green scatter) under $V_{ds} = 0.5$ V; The dependence of I_{gs} on V_{gs} before (black curve) and after FGA (green curve) is also presented. Static figures of (b) SS ratio and (c) μ_{eff} ratio between transistors after and before FGA; (d) Output curves for as-fabricated transistor (black curves) under $V_{gs} - V_{th} = -2.1 \sim -1.9$ V and transistor after FGA (green curves) under $V_{gs} - V_{th} = -2.0 \sim -2.0$ V.

Figure 2(a) compares the typical transfer curves of ML MoS₂ transistor before (black scatter) and after (red scatter) TFSI treatment under $V_{ds} = 0.5$ V. After TFSI treatment, the V_{th} shifts negatively from -1.0 to -1.25 V. The minimum SS of the device decreases from 280 to 230

mV/dec. The μ_{eff} of ML MoS₂ is improved from 0.41 to 1.01 cm²·V⁻¹·s⁻¹. Figure 2(b) displays the static figure of SS ratio between transistors after and before TFSI treatment along with a Gaussian simulation curve (red). The peak value of the SS ratio is around 0.86 verifying that the gate controllability of ML MoS₂ device is enhanced after TFSI treatment. Figure 3(c) further gives the static figure of μ_{eff} ratio between transistors after and before TFSI treatment along with corresponding Gaussian simulation curve (red curve). The peak value of the μ_{eff}

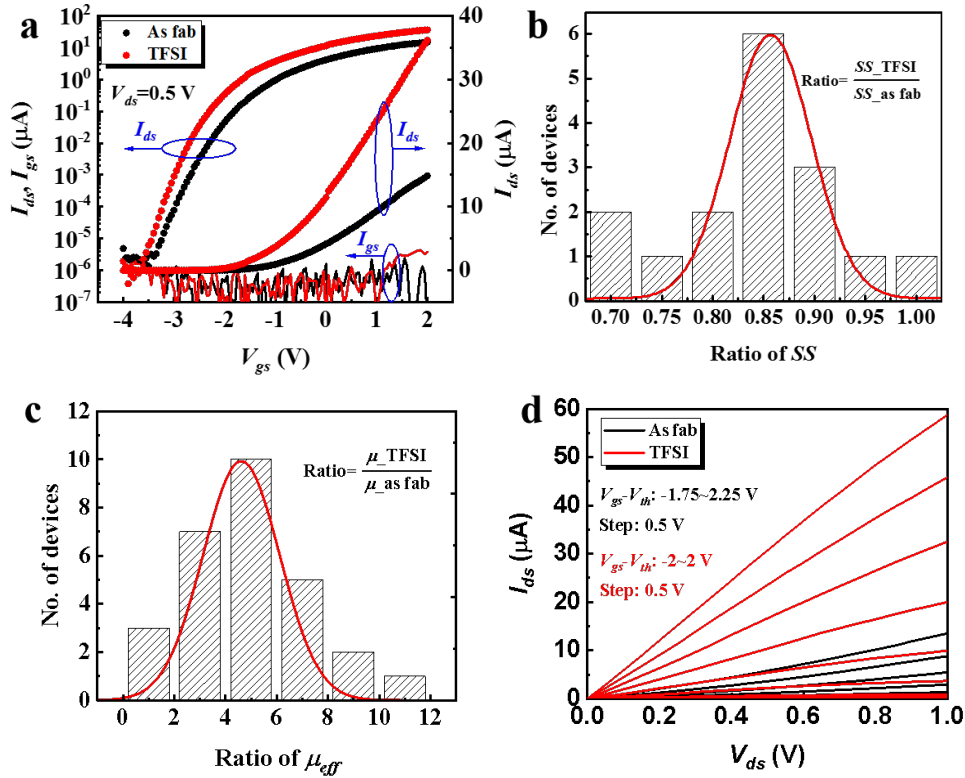


Fig. 2. (a) Comparison of transfer curves for ML top-gated MoS₂ transistor before (black scatter) and after (red scatter) TFSI treatment in semi-log and linear scales under $V_{ds}=0.5$ V; The dependence of I_{gs} on V_{gs} before (black curve) and after (red curve) FGA is also presented. Static figure of (b) SS ratio and (c) μ_{eff} ratio between transistors after and before TFSI treatment; (d) Output curves for as-fabricated transistor (black curve) under $V_{gs}-V_{th}=-1.75\sim 2.25$ V and transistor after TFSI treatment (red curve) under $V_{gs}-V_{th}=-2.0\sim 2.0$ V.

ratio is around 4.5 confirming that the μ_{eff} of ML MoS₂ is effectively improved after TFSI treatment. Figure 2(d) shows the output curves for presented ML MoS₂ transistor before (black curves) and after TFSI treatment (red curves). The much larger slope of I_{ds}/V_{ds} in device after TFSI treatment manifest that the device resistance is effectively reduced after TFSI treatment.

Linear transmission-line-model (TLM) [6] measurements were carried out to measure the change of contact resistance (R_c) between Ti and ML MoS₂ and the change of sheet resistance

R_s of ML MoS₂ after different treatments. The width (W) of the MoS₂ TLM structure is 10 μm , the spacing of adjacent pads (l_d) in the linear TLM structure varies from 0.4 to 2 μm . Through measuring the total resistance (R) between adjacent pads, R_s and R_c can be extracted from linear fitting the R - l_d curve. Figure 3(a) compares the dependence of R on l_d from linear TLM structures before (black scatter) and after FGA (green scatter). It is found that R_c reduces greatly from 12.2 to 4.57 k Ω , while R_s reduces slightly from 950 to 750 k Ω/\square after FGA. Fig. 3(b) compares the dependence of R on l_d from linear TLM structures before (black scatter) and after TFSI treatment (red scatter). It is found that R_c reduces slightly from 11.5 to 9.0 k Ω , while R_s reduces significantly from 850 to 143 k Ω/\square after TFSI treatment. The results manifest that R_c and R_s both reduce after FGA and TFSI treatment. However, post FGA is preferable in reducing the R_c between Ti and ML MoS₂, while post TFSI treatment is more effective in reducing the R_s of ML MoS₂.

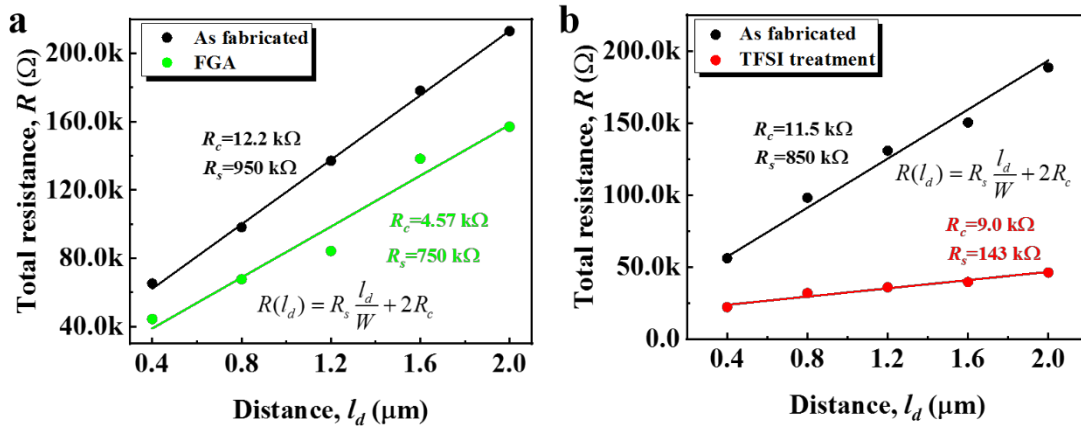


Fig. 3. Dependence of R on l_d measured from linear TLM structures for ML MoS₂ before and after FGA; (b) Dependence of R on l_d measured from linear TLM structures for ML MoS₂ before and after TFSI treatment. Through linear fitting of R - l_d by equation (3), R_c and R_s can be extracted from the intercept and slope, respectively.

1.2 Raman spectra of HfO₂-capped ML MoS₂ after post treatment

Figure 4 compares the Raman spectra of HfO₂-capped ML MoS₂ without post treatment (black curve), after FGA (green curve) and after TFSI treatment (red curve). Peaks at around 385 and 403 cm^{-1} come from the in-plane E_{2g}^1 and the out-plane A_{1g}^1 modes, respectively.

After FGA, E_{2g}^1 mode downward shifts, while A_{1g}^1 mode upward shifts suggesting that

defects are induced into MoS₂ [7]. An obvious tailing (blue dash circles) on the lower wavenumber side of E_{2g}^1 mode is observed with an increasing FWHM, which is a signature of introduction of disordered lattice structure in MoS₂ [8]. As reported, S atoms can be removed by H₂ in the form of H₂S under H₂ annealing at low temperature leading to formation of S vacancies along with mid-gap (deep) states by the under-coordinated Mo atoms [9, 10]. Thus, the defects generated during FGA can be attributed to S vacancies. The introduction of S vacancies and under-coordinated Mo atoms increases the *n*-type doping concentration and *SS*. After TFSI treatment, the downward shifting and broadening of E_{2g}^1 and A_{1g}^1 modes indicate a doping effect in MoS₂ [11]. The dissolved TFSI in DCB solution contains abundant TFSI anions and nearly-free protons (H⁺). During post treatment of MoS₂ with TFSI solution, H⁺ can penetrate through the gate dielectric [12] and laterally hops in MoS₂ [13]. The H⁺ binding at S vacancies can trap electrons leading to increase of the *n*-type doping concentration in MoS₂. Additionally, the penetrating H⁺ has a passivation effect on defects at dielectric/MoS₂ interface making contribution to the reduction of *SS*.

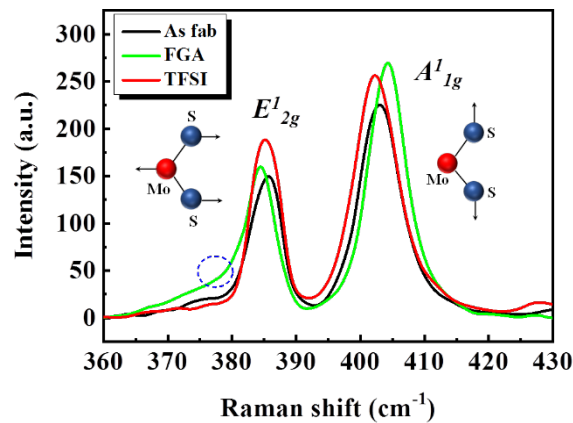


Fig. 4. Comparison of Raman spectra from HfO₂-capped ML MoS₂ without post treatment (black curve), after FGA (green curve) and after TFSI treatment (red curve).

1.3 XPS spectra of HfO₂-capped ML MoS₂ after post treatment

Figures 5(a)~6(d) show the XPS spectra of Mo 3*d*, S 2*p*, Hf 4*f* and O 1*s* chemical states taken from 3-nm-HfO₂-capped MoS₂ without post treatment (black curve), after FGA (green curve) and after TFSI treatment (red curve), respectively. The origin of each peak has been

labelled. The atomic ratio between Mo and S (R_{Mo-S}) for HfO₂-capped MoS₂, HfO₂-capped MoS₂ after FGA and TFSI treatment is calculated as 1:1.93, 1:1.91 and 1:1.94, respectively. The decrease of R_{Mo-S} after FGA corroborates

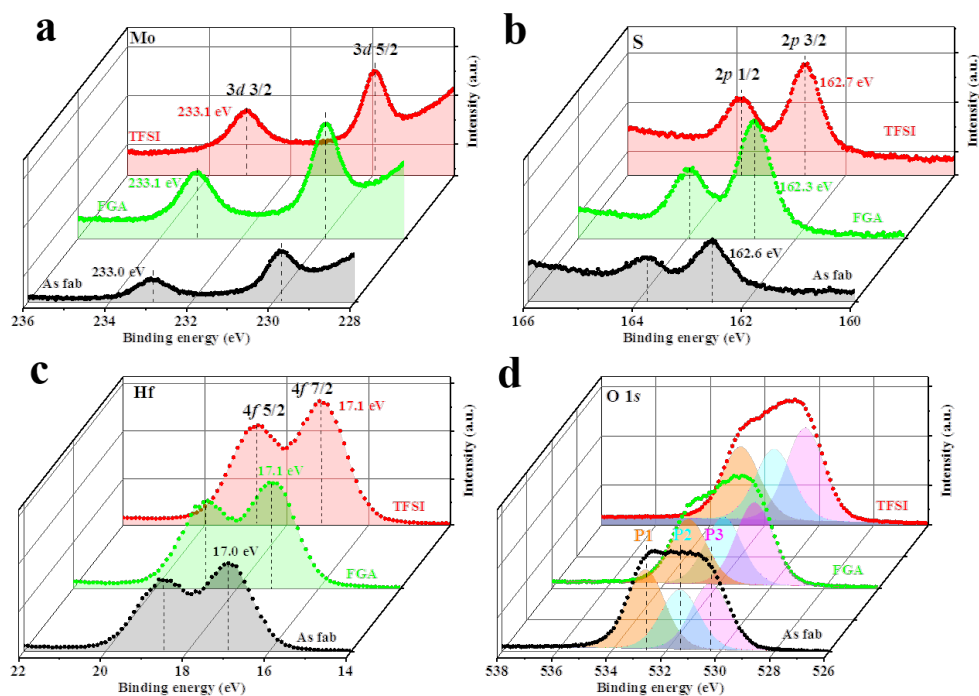


Fig. 5. XPS spectra of (a) Mo 3d, (b) S 2p, (c) Hf 4f and (d) O 1s core levels taken from HfO₂-capped MoS₂ (black curves), HfO₂-capped MoS₂ after FGA (green curves) and TFSI treatment (red curves).

introduction of S vacancies. The O 1s spectra can be resolved into 3 peaks: P1 at around 532.7 eV excited from Si-O [14] and H-O [15] bonds, P2 at around 531.4 eV excited from Al-O [14] bonds and P3 at around 530.4 eV excited from Hf-O [13] bonds. The area ratio of P1 peak decreases significantly from 0.39 to 0.30 and 0.31 after FGA and TFSI treatment, respectively. And the P1 peak area ratios for HfO₂-capped MoS₂ after FGA and TFSI treatment are almost the same. Since the P1 peak is an overlap signal from Si-O and H-O bonds and the signal from Si-O after different treatments should not change in principle, the results indicate that water molecules desorb from the HfO₂-capped MoS₂ structure after FGA and TFSI treatment. The remove removal of water on MoS₂ improves μ_{eff} and also contributes to the negative shift of V_{th} .

In summary, after FGA and TFSI treatment, a negative shift of V_{th} is observed and the μ_{eff}

can be effectively improved (to ~ 1.6 and ~ 4.5 folds, respectively). However, FGA would result in an increase of SS (to ~ 1.5 folds), while TFSI treatment can effectively reduce the SS (to ~ 0.86 folds). It is found that post FGA is preferable in reducing the R_c between Ti and ML MoS₂, while post TFSI treatment is more effective in reducing the R_s of ML MoS₂. Raman and XPS measurement results reveal that water desorbs from MoS₂ after FGA and TFSI treatment and S vacancies are introduced into MoS₂ after FGA. The results manifest that post TFSI treatment provides a simple and effective approach to improve the electrical property of MoS₂ and may be a general strategy to improve or recover the electrical performance of other S-containing 2D TMDs.

2. InAs FinFETs Performance Enhancement by TFSI Treatment

To the extend application field of the method, TFSI treatment was further carried out for InAs FinFETs. Enhancement of electron mobility and gate controllability were also observed after TFSI treatment showing a good potential of TFSI treatment in enhancing the electrical performance of III-V MOSFETs.

The effectiveness of TFSI treatment in improving the electrical performance of MoS₂ transistors has been demonstrated. To the extend application field of the method, TFSI treatment was carried out for InAs FinFETs for the first time. The low field-effect mobility was observed to increase by 5.8~7.1 folds reaching 671~1378 cm²·V⁻¹·s⁻¹. The results suggest that TFSI treatment can be potentially extended to III-V MOSFETs to enhance the device performances.

2.1 InAs FinFET fabrication and TFSI treatment

The InAs FinFETs were fabricated from InAs ribbons on SiO₂/Si substrate, which were obtained by transfer method [16]. By e-beam lithography (EBL) and inductively coupled plasma (ICP) dry etching methods, fins with length of 1 μ m and widths of 20 and 25 nm were formed along the InAs ribbons. Ni/Au (40 nm/15 nm) was then evaporated as source (S) and drain (D) contacts. After that 8-nm ZrO₂ was deposited as gate oxide by ALD. Ultimately, 50-nm Ni was selectively evaporated as gate (G) metal. To carry out TFSI treatment, 0.2 mg/ml TFSI solution was prepared in glove box [4]. The InAs FinFETs were immersed in the 0.2-

mg/ml solution for 20 s at air ambient, then blow-dried with N₂.

2.2 Electrical performance of InAs FinFET before and after TFSI treatment

Figure 6 shows typical transfer characteristics (I_{ds} - V_{gs}) of the FinFET with fin width of 25 nm before and after TFSI treatment at V_{ds} =0.05 V (Fig. 6(a)) and V_{ds} =0.5 V (Fig. 6(b)), respectively. After TFSI treatment, both the on/off ratio and on-current increase significantly. At V_{ds} =0.05 V, the on/off ratio increases from 2.35×10^3 to 8.18×10^3 (~3.5x), the on-current increases from 0.20 to 1.56 $\mu\text{A}/\mu\text{m}$ (~7.8x); At V_{ds} =0.5 V, the on/off ratio increases from 1.51×10^3 to 12.1×10^3 (~8x), the on-current increases from 1.30 to 13.15 $\mu\text{A}/\mu\text{m}$ (~10x). After TFSI treatment, the hysteresis phenomenon is less pronounced. Additionally, the extracted subthreshold swing (SS) is reduced from 217 to 170 mV/dec. The reduction of SS suggests that the density of interfacial traps (D_{it}) is effectively reduced after the TFSI treatment. The D_{it} can be quantitatively calculated based on the following equation: [17]

$$\frac{2.3kT}{q} \left(1 + \frac{C_{it}}{C_{ZrO_2}} + \frac{C_{body}}{C_{ZrO_2}} - \frac{\frac{C_{body}^2}{C_{ZrO_2} + C_{SiO_2}}}{1 + \frac{C_{it}}{C_{SiO_2}} + \frac{C_{body}}{C_{SiO_2}}} \right) = SS, \quad (1)$$

where k , T , and q is Boltzmann constant, sample temperature and elementary charge, respectively; C_{ZrO_2} , C_{SiO_2} and C_{body} represents the capacitance of ZrO₂, SiO₂ and the substrate per unit area, respectively; C_{it} is the capacitance caused by interface traps per unit area and is given by $C_{it}=qD_{it}$. For the presented device, D_{it} has reduced from $1.21 \times 10^{13} \text{ cm}^{-2}$ before TFSI treatment to $7.91 \times 10^{12} \text{ cm}^{-2}$ after TFSI treatment. The calculated D_{it} along with SS before and after TFSI treatment for several different devices were summarized in Table I. For all devices, both of SS and D_{it} values reduce distinctly after TFSI treatment indicating the passivation effect of TFSI on interfacial traps.

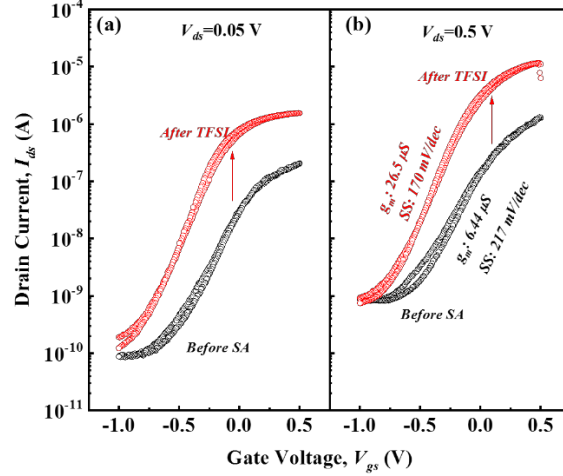


Fig. 6. Typical transfer characteristics of the InAs FinFETs with fin width of 25 nm before (black curve) and after TFSI (red curve) treatment under (a) $V_{ds}=0.05$ and (b) $V_{ds}=0.5$ V. A large current increase and steeper SS after TFSI treatment can be observed.

Table I. Summary of SS and D_{it} for different devices before and after TFSI treatment.

Device ($L_g=1 \mu\text{m}$)		SS (mV/dec)	D_{it} (cm^{-2})
$W_{fin}=25 \text{ nm}$	Before TFSI	156	6.74×10^{12}
	After TFSI	130	4.69×10^{12}
$W_{fin}=25 \text{ nm}$ (presented)	Before TFSI	217	1.21×10^{13}
	After TFSI	170	7.91×10^{12}
$W_{fin}=20 \text{ nm}$	Before TFSI	98	2.40×10^{12}
	After TFSI	70	6.20×10^{11}
$W_{fin}=20 \text{ nm}$	Before TFSI	530	4.43×10^{13}
	After TFSI	170	8.76×10^{12}

To further characterize the influence of TFSI treatment on the sheet resistance (R_s) of InAs and contact resistance (R_c) between InAs and Ni/Au, linear-transmission-line-model (TLM) measurements were conducted. Electrodes with different gap spacing (l_d) were fabricated along the InAs ribbons on SiO_2/Si substrate, as shown in the inset of Fig. 7. The width of the ribbon is $4 \mu\text{m}$ (W) with contact areas of $4 \times 4 \mu\text{m}^2$. Figure 7 shows the measured values of R under different l_d along with corresponding fitting results before and after TFSI treatment. The measured results reveal that R_s had reduced from 652.1 to $501.5 \Omega/\square$, while R_c remained almost same at 30.5Ω after SA treatment suggesting enhancement of the InAs mobility due to

reduction of D_{it} .

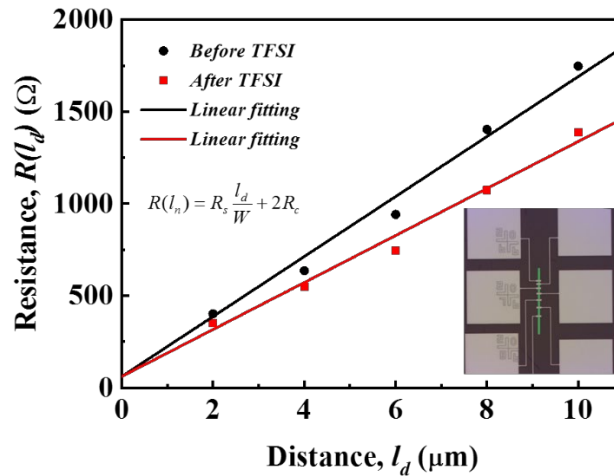


Fig. 7. Resistance (R) between adjacent pads as a function of gap spacing (l_d) from TLM measurements before (black) and after (red) TFSI treatment.

2.3 XPS spectra of ZrO_2 -capped InAs before and after TFSI treatment

To shed light on passivation mechanisms of the interfacial traps after TFSI treatment, high-resolution XPS measurements were carried out. Figures 8(a)-(c) display the XPS spectra of O 1s, As 3d and In 3d 5/2 of ZrO_2 -capped InAs before TFSI treatment, respectively. The corresponding results after TFSI treatment are shown in Figs. 8(a')-(c'), respectively. The origin of each subpeak has been fitted and labelled. It is concluded that the intensity of AsO_x remains almost constant after TFSI treatment, while the intensity of In_2O_3 and ZrO_2 reduces evidently. From the XPS spectra of O 1s core level, it is found that the integral intensity ratio between AsO_x and In_2O_3 has increased from 0.98 before TFSI treatment to 1.38 after TFSI treatment. The results manifest that the interfacial oxide at the InAs/ ZrO_2 interface, especially In_2O_3 , is effectively reduced after TFSI treatment.

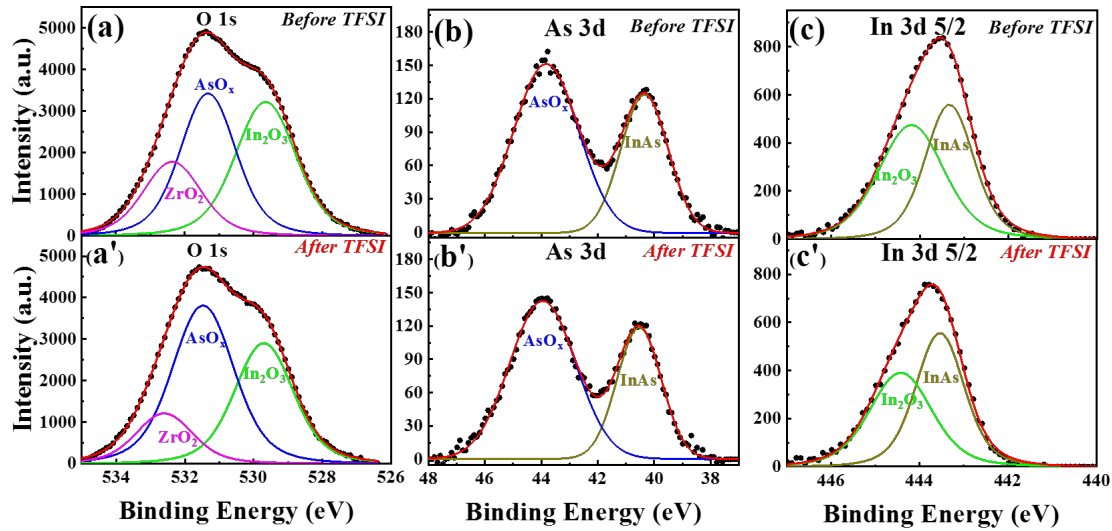


Fig. 8. XPS spectra of (a) O 1s, (b) As 3d and (c) In 3d 5/2 and related fitting results for ZrO₂-capped InAs before TFSI treatment; XPS spectra of (a') O 1s, (b') As 3d and (c') In 3d 5/2 and related fitting results for ZrO₂-capped InAs after TFSI treatment.

2.4 BSIM model fitting for mobility extraction

To further investigate the effect of TFSI treatment on the carrier mobility of InAs FinFETs, we have modeled I - V characteristics before and after TFSI treatment based on industry standard compact model BSIM-CMG [18]. For our goal of finding an estimated improvement of carrier mobility after SA treatment, we consider that parasitic series resistance between source and drain (R_{ds}) falls in the range of 10% to 95% of device total resistance (R_{total}) at the highest V_{gs} ($V_{gs}=0.5$ V). The consideration follows from a practical reasoning that a value of R_{ds} larger than 95% of R_{total} would require nonphysical channel mobility to explain experimental drain current. With this range of R_{ds} , we have modeled the I_{ds} - V_{gs} characteristics of the InAs FinFETs before and after TFSI treatment taking R_{ds} 10-95% of R_{total} , as shown in Figs. 9(a). Under V_{gs} of 0.5 V, the carrier mobility before TFSI treatment is estimated to be 114~195 cm²·V⁻¹·s⁻¹. After TFSI treatment, the carrier mobility is increased to 671~1378 cm²·V⁻¹·s⁻¹, about 5.8~7.1 folds enhancement. The extracted mobility values are validated by modeling the saturated transfer characteristics of InAs FinFET under V_{ds} of 0.5 V taking R_{ds} 10~95% of R_{total} . The modeled saturation I_{ds} - V_{gs} curves are presented in Fig. 9(b), which agree very well with the experimental data.

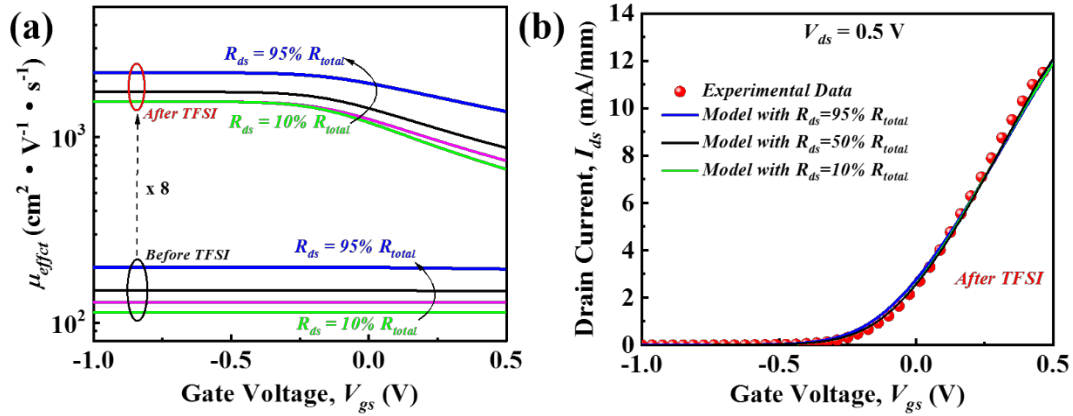


Fig. 9. (a) Extracted effective carrier mobility (μ_{effect}) of InAs FinFETs versus V_{gs} before and after TFSI treatment by I_{ds} - V_{gs} modeling based on BSIM-CMG model. The modeling was performed taking R_{ds} 10~95% of R_{total} . (b) Modeling of the saturation transfer characteristics of InAs FinFETs under V_{ds} of 0.5 V taking R_{ds} 10~95% of R_{total} .

In summary, post TFSI treatment was carried out for InAs FinFETs. For the reported device, the SS has reduced from 217 to 170 mV/dec. Through XPS analysis, it was found that the interfacial oxide at the InAs/ ZrO_2 interface was effectively reduced after TFSI treatment due to strong protonating nature of SA solution. From modeling of the transfer characteristics based on the commercial BSIM-CMG model, it was found that the carrier mobility is enhanced from 114~195 $cm^2V^{-1}\cdot s^{-1}$ before TFSI treatment to 671~1378 $cm^2 V^{-1}\cdot s^{-1}$ after TFSI treatment due to reduction of interfacial traps. The results suggest that TFSI treatment can be potentially extended to III-V MOSFETs to enhance the device performances.

3. TiO_2 thin film transistor performance enhancement by superacid treatment

Metal oxide thin film transistors (TFTs) promise to enable a wide range of applications, such as high-resolution display and RF identification tags. To meet the requirements of these applications, TFTs with enhanced current drivability are highly desirable. Traditional chemical doping for improving TFT on-current usually requires complicated synthesis mechanism and expensive growth equipment. In addition, the inherent structure disorder from chemical doping may also decrease carrier mobility [19]. In this regard, a simple doping method of boosting current drivability without distorting material structure is much appreciated. Herein, we report for the first time on a simple, equipment-free, air-ambient, room-temperature, solution-based superacid (SA) treatment to enhance the current drivability of TiO_2 TFTs. The on-current is

found to be enhanced by nearly 2x via a quick dip in SA solution.

3.1 Device Fabrication

Figures 10 illustrate the schematic and microscope views of TiO₂ TFTs. These TiO₂ TFTs are formed in a top-gate structure with source/drain offsets. The fabrication process is reported in our previous work [20]. The gate width (W_G), gate-drain offset (L_{GD}), gate-source offset (L_{GS}) and gate length (L_G) of TiO₂ TFTs is 70, 1.5, 1.5 and 2.5 μm , respectively. The channel material, gate dielectric, S/D metal and gate metal are respectively 15 nm TiO₂, 10 nm ZrO₂, 250 nm Al and 170 nm Ni /80 nm Au. Both TiO₂ and ZrO₂ are grown by atomic layer deposition (ALD). Two samples with TiO₂ TFTs of same dimensions are prepared and dipped into 0.2 mg/mL bis(trifluoromethane) sulfonamide (TFSI) solution (so called ‘SA’) and 1-ethyl-3-methylimidazolium bis(trifluoromethylsulfonyl)imide (EMIm TFSI) solution, respectively. The samples were dipped for 20 s at room temperature with air ambient and blow dried with N₂ right after being removed from solutions. It is noted that two solutions are of the same concentration, anion and solvents (1,2-dichloroethene and 1,2-dichlorobenzene) with the only difference in the cations. The chemical structures of SA and EMIm TFSI are shown in Fig.11.

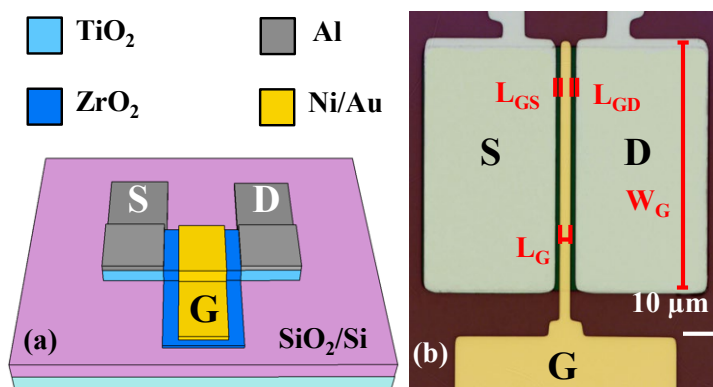


Fig. 10 (a) Schematic view and (b) microscope view of TiO₂ TFTs.

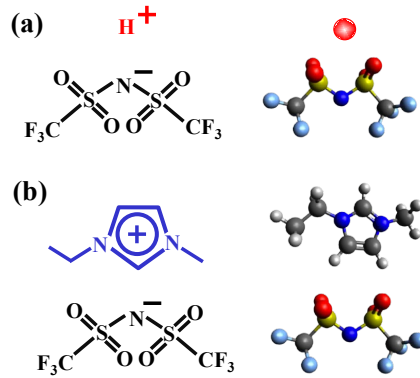


Fig. 11. Chemical structure of (a) TFSI (Superacid) and (b) EMIm TFSI.

3.2 Electrical characterizations

The electrical properties of TiO_2 TFTs before and after treatments were measured using an Agilent B1500A semiconductor parameter analyzer. Figures 12 show the transfer curves and gate leakage at $V_{\text{DS}} = 10$ V for devices before and after SA and EMIm TFSI treatment. It is shown that SA-treated TFTs exhibit an enhanced on-current in contrast to that a decrease in on-current can be observed in the EMIm TFSI-treated TFTs. Both treated-TFTs show similar fast switching behaviors with subthreshold swing of ~ 120 - 130 mV/dec and the same gate leakage current level (at $\sim 10^{-12}$ A) as the as-fabricated TFTs. This may be due to the fact that, the $\text{ZrO}_2/\text{TiO}_2$ channel interface is mostly encapsulated by top-gate metal, leading to the less influence by the post-treatment. A negative shift threshold voltage and an increased off-current can be observed in SA-treated TFTs, possibly indicating that an ion conduction mechanism exists in addition to electron conduction in SA-treated TFTs [21]. The corresponding output characteristics of two devices are depicted in Fig.13, where the current enhancement due to SA treatment is distinct. The Schottky contact behaviors can also be observed in the linear region of both TFTs, possibly due to that the Al metals are attacked by treatments arising from the acid nature of both solutions.

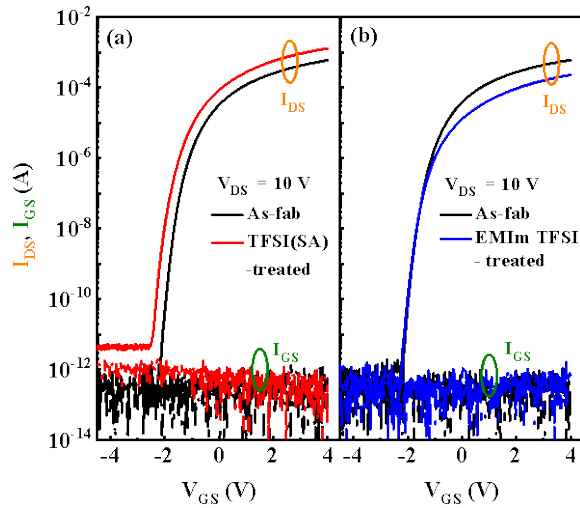


Fig. 12. Transfer curves and gate leakage at $V_{DS} = 10$ V for devices before and after (a) SA treatment and (b) EMIm TFSI treatment.

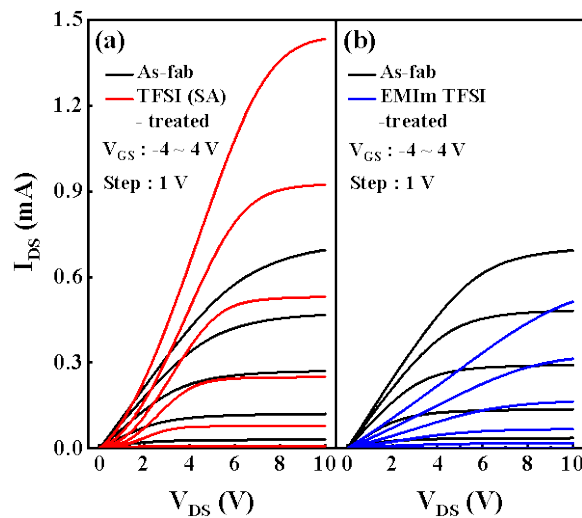


Fig. 13. Output characteristics for devices before and after (a) SA treatment and (b) EMIm TFSI treatment.

Figure 14 shows the statistical results of current change, defined as the current ratio before and after treatment at $V_{DS} = 10$ V and $V_{GS} = 4$ V biasing condition, among 13 SA-treated TFTs and 10 EMIm TFSI-treated TFTs with the same dimensions. The SA-treated TFTs show a nearly 2x current enhancement in contrast to that of a $\sim 20\%$ current decrease in EMIm TFSI-treated TFTs. The current drop in the EMIm TFSI-treated TFTs can be explained by the formation of the Schottky barrier between Al S/D metal and TiO_2 , which would hinder the electron injection and extraction process. Despite of Schottky behaviors observed in both TFTs, such current increase after SA treatment indicates the existing of a strong current boosting mechanism,

concealing the detrimental effects from Schottky contacts.

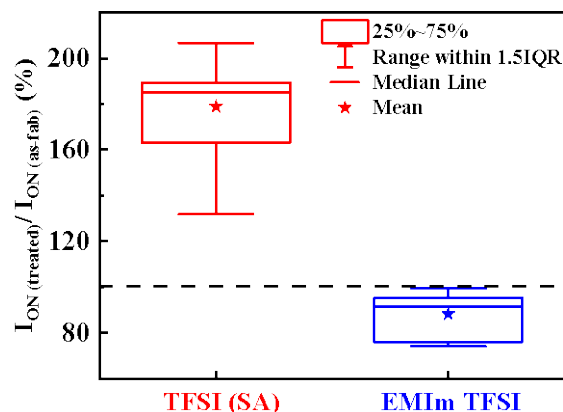


Fig. 14. Statistical results of current changes based on 13 SA-treated TFTs and 10 EMIm TFSI-treated TFTs with same dimensions.

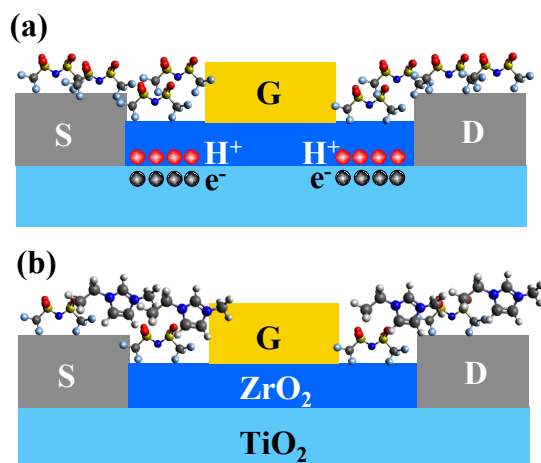


Fig. 15. Schematic illustration of the mechanism in (a) SA treatment and (b) EMIm TFSI treatment on TiO_2 TFTs.

The possible mechanisms of SA and EMIm TFSI treatment on TiO_2 TFTs are schematically depicted in Fig.15. SA is a well-known protonating agent with abundant labile hydrogen [22]. It is believed the current enhancements originate from the protons in SA solutions. Protons (H^+), with small ionic radius of 25 pm, may penetrate the ZrO_2 in the TFT offset region and accumulate at the $\text{ZrO}_2/\text{TiO}_2$ interface, forming an electron-double-layer and n-doping the offset region in TFTs [21]. In contrast, the TFSI anion and EMIm cations, with large ionic radius of 0.9 nm and 0.8 nm, respectively [23], may be blocked by ZrO_2 and thus have less influences on the TFT performance.

In summary, SA treatment is shown as effective method to enhance the current drivability of TiO₂ TFTs by ionic doping of the offset region. We believe this simple, equipment-free, air-ambient and room-temperature doping method could provide more functionalities and flexibilities for future TFT applications.

4. Superacid treatment on GaN high electron mobility transistors

PI's group has recently demonstrated record high performance GaN-on-Si high electron mobility transistors. In order to further enhance the device performance, superacid treatment was applied after device completion.

4.1 Device fabrication

Figure 16 shows the schematic of the fabrication process for InAlN/GaN HEMT on Si substrate. The InAlN/GaN heterostructure consists of 2-nm GaN cap layer, an 8-nm lattice-matched In_{0.17}Al_{0.83}N barrier layer, a 1-nm AlN interlayer, a 15-nm GaN channel layer, a 4-nm In_{0.12}Ga_{0.88}N back barrier layer, and a 2- μ m undoped GaN buffer layer on a Si substrate. This structure is grown by metalorganic chemical vapor deposition (MOCVD). The sheet electron concentration and electron mobility measured by Hall measurements were $2.28 \times 10^{13} \text{ cm}^{-2}$ and $1205 \text{ cm}^2/\text{V}\cdot\text{s}$, respectively.

The device fabrication process started with mesa formation by Cl₂/CH₄/He/Ar inductively coupled plasma etching (ICP) and the etching depth is $\sim 300 \text{ nm}$. Alloyed ohmic contact of Ti/Al/Ni/Au metal stack was then deposited by electron-beam (e-beam) evaporation, followed by annealing at 850°C for 40s in N₂. The source-drain distance (L_{SD}) is 15 μm . Subsequently, the sample surface was treated with oxygen plasma treatment using Allwin21 O₂ Plasma Asher. The RF power of 800W was applied for 1 min to form an oxide layer on the surface of InAlN layer, which acts as the gate dielectric and device passivation layer. The resulted oxide layer on the surface can effectively reduce the gate leakage current and improve device performance. Then, the gate schottky contact was formed in the center of the source and drain ohmic contacts with photolithography followed by Ni/Au metal deposition. The gate length (L_G), gate-source spacing (L_{GS}) and the gate-drain spacing (L_{GD}) are all 5 μm . Finally, the surperacid (SA) surface treatment is applied on the whole chip. An organic SA, bis (trifluoromethane) sulfonamide (TFSI), which is a strong protonating agent and have a Hammett acidity function that is lower

than pure sulfuric acid (H_2SO_4), was prepared in a glove box for surface treatment on the completed InAlN/GaN HEMTs. To prepare the TFSI solution, 24 mg TFSI powder was first dissolved in 12 mL 1, 2-dichloroethene (DCE) to form TFSI solution with solute concentration of 2 mg/mL; then 0.5 mL of the 2 mg/mL TFSI solution was diluted with 4.5 mL 1, 2-dichlorobenzene (DCB) forming a 0.2 mg/mL TFSI solution. The InAlN/GaN HEMTs were immersed in the 0.2 mg/mL solution for 20 s at air ambient, then blow-dried with N_2 . Both the device performances before and after SA treatment were measured using an Agilent B1500A semiconductor parameter analyzer to compare the effects of the SA on the InAlN/GaN HEMTs.

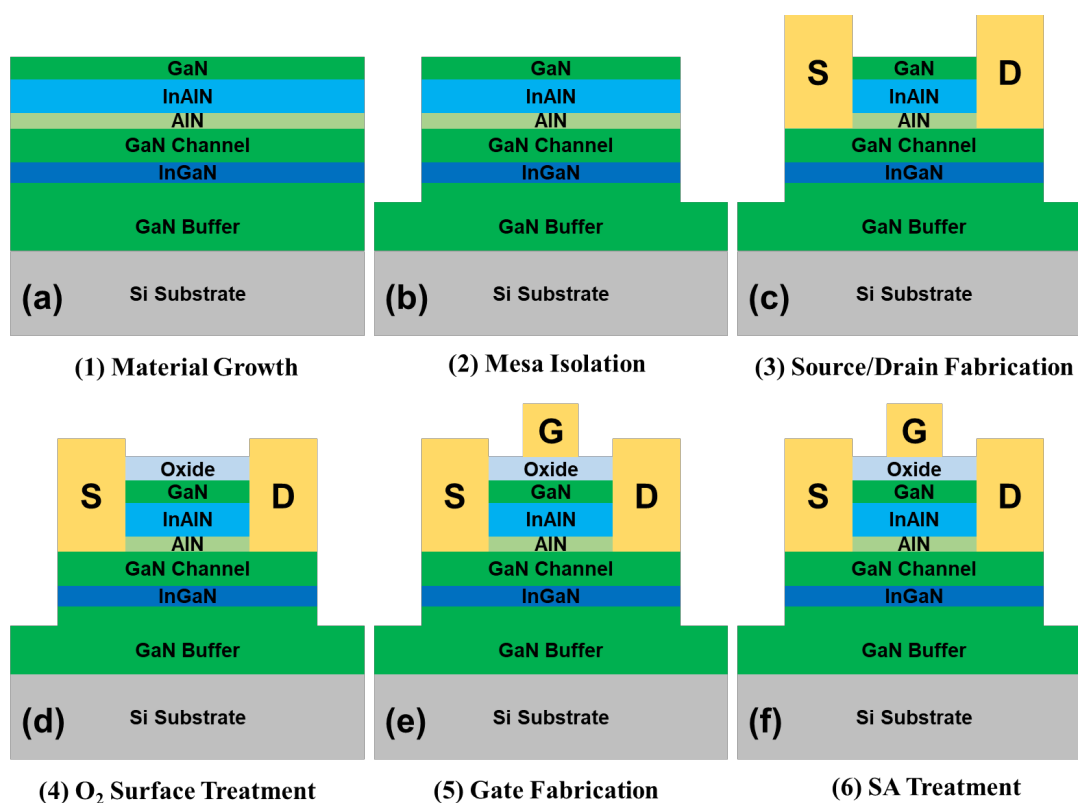


Fig. 16 Schematic of the fabrication process for InAlN/GaN HEMT on Si substrate: (a) Material Growth, (b) Mesa Isolation, (c) Source/Drain Fabrication, (d) O_2 Surface Treatment, (e) Gate Fabrication. (f) Superacid surface Treatment.

4.2 Electrical characterizations

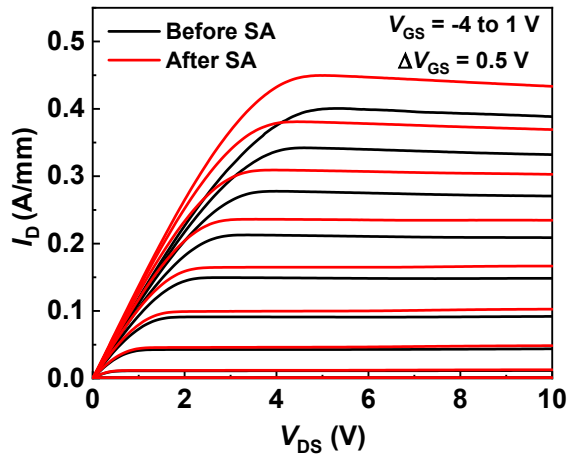


Fig. 17. I - V output characteristics of InAlN/GaN HEMT before and after SA treatment.

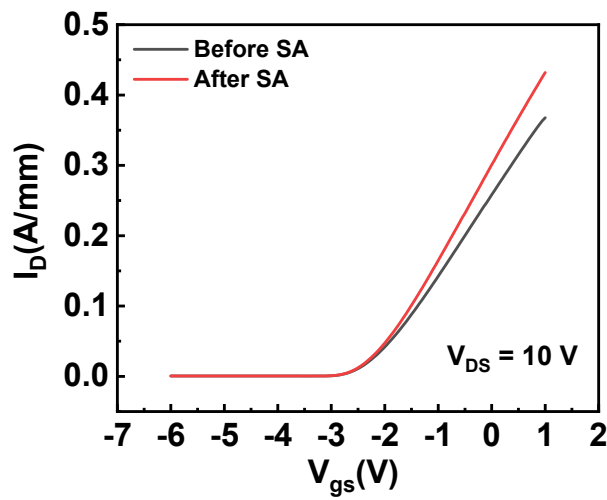


Fig. 18. Transfer characteristics at $V_{DS} = 10$ V of InAlN/GaN HEMT before and after SA treatment.

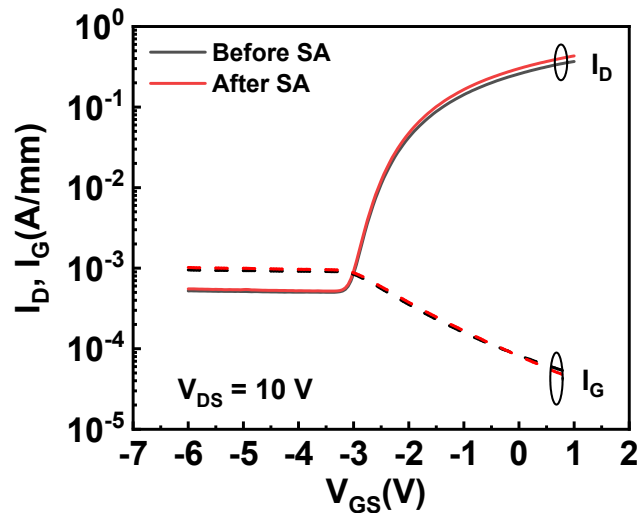


Fig. 19. Transfer characteristics in log-scale at $V_{DS} = 10$ V of InAlN/GaN HEMT before and after SA treatment.

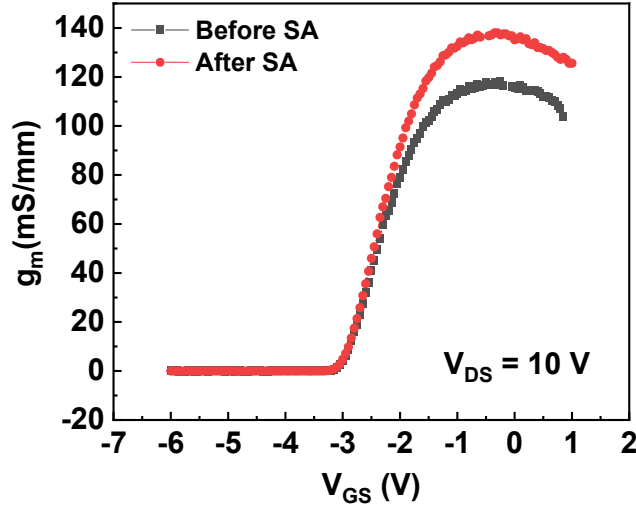


Fig. 20. Transconductance at $V_{DS} = 10$ V of InAlN/GaN HEMT before and after SA treatment.

Figure 17 shows the I - V output characteristics of the InAlN/GaN HEMT before and after SA treatment. The on-resistance (R_{on}) is extracted at the gate-source voltage (V_{GS}) of 0 V and drain-source voltage (V_{DS}) between 0 V and 0.5 V. It is found R_{on} decreases from $8.74 \Omega \cdot \text{mm}$ (before SA) to $7.72 \Omega \cdot \text{mm}$ (after SA). The transfer characteristics at $V_{DS} = 10$ V are measured and plotted in Fig. 18. The on-current increases from 0.36 A/mm (before SA) to 0.43 A/mm (after SA). The correspond transfer characteristics in logscale are plotted in Fig. 19. The on/off ratio (I_{ON}/I_{OFF}), subthreshold swing (SS), and gate leakage current (I_G) are almost unchanged after SA surface treatment. Figure 20 exhibits the transconductance (g_m) at $V_{DS} = 10$ V. With SA treatment, the peak of g_m increases from 118 mS/mm to 138 mS/mm.

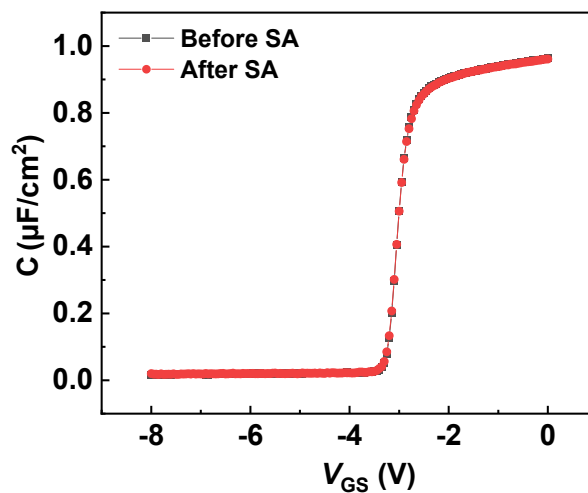


Fig. 21. Measured gate capacitance of InAlN/GaN HEMT before and after SA treatment.

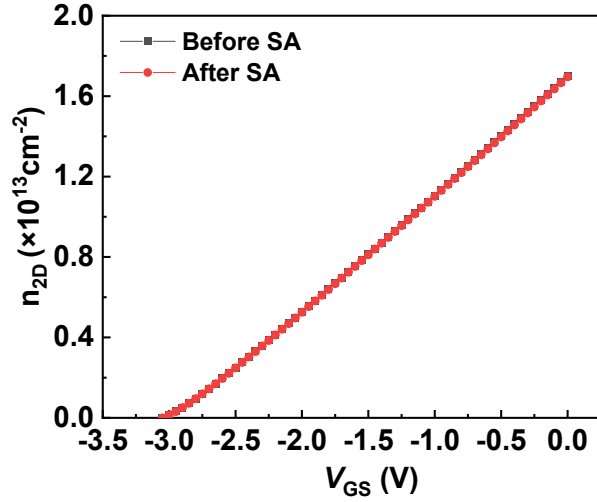


Fig. 22. Two-dimensional electron gas electron density (n_{2D}) of InAlN/GaN HEMT before and after SA treatment.

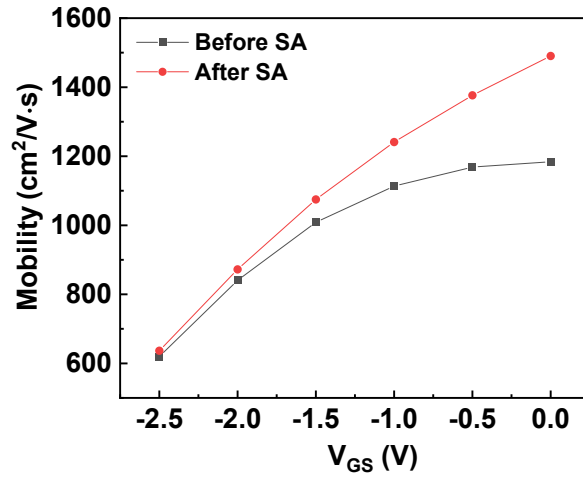


Fig. 23. Electron mobility under the gate region of InAlN/GaN HEMT before and after SA treatment.

In order to shed more light on the effect of SA treatment, the gate capacitance versus the gate-source voltage V_{GS} of both samples was measured as shown in Fig. 21. By integrating the measured C - V curves, the two-dimensional electron (2DEG) electron density (n_{2D}) under different gate biases can be obtained as shown in Fig. 22. It is shown that both the gate capacitance and the n_{2D} are almost unchanged with SA surface treatment. Based on the measured I - V characteristic and the n_{2D} , the 2DEG electron mobility under the gate region can be calculated as follows

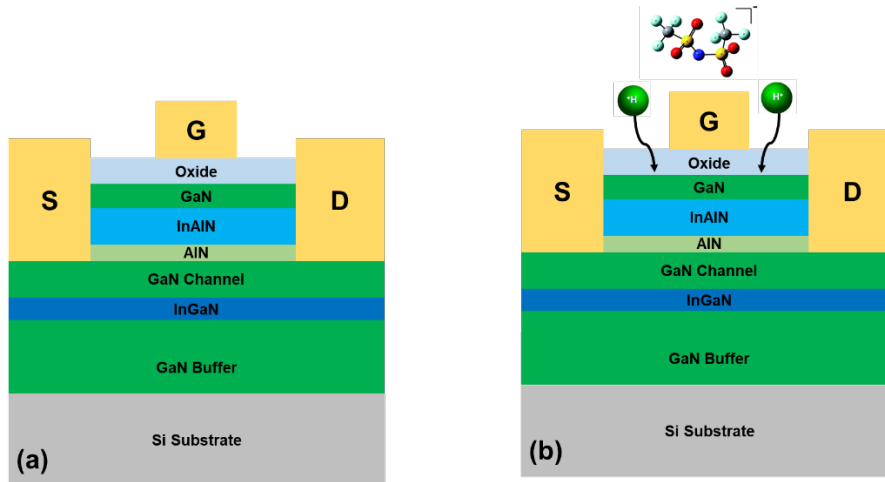
$$\mu_n = \frac{L_G}{qn_{2D}W_G[V_{DS}/I_{DS} - (R_D + R_S)]}, \quad (1)$$

$$R_D = \frac{L_{GD}}{qn_{2D0}\mu_{n0}W_G}, \quad (2)$$

$$R_S = \frac{L_{GS}}{qn_{2D0}\mu_{n0}W_G}. \quad (3)$$

Here, q is the electron charge, V_{DS} and I_{DS} are the applied drain-source voltage and current, respectively. R_D is the drain access resistance, and R_S is the source access resistance. n_{2D0} and μ_{n0} are the 2DEG sheet density and 2DEG electron mobility when the gate-source voltage is 0 V. In order to minimize the effect of the drain-source voltage on the channel under the gate region, the 2DEG electron mobility at low drain-source bias ($V_{DS} = 0.1$ V) are calculated, as shown in Fig. 23. It is observed that the electron mobility is improved with SA surface treatment.

Electron mobility is determined by the scattering mechanisms in InAlN/GaN HEMTs. Polar optical phonon (POP), acoustic phonon (AP), interface roughness (IFR), dislocation (DIS), and polarization Coulomb field (PCF) scatterings are the main scattering mechanisms in InAlN/GaN HFETs. Because the electron density is almost unchanged, the former four scatterings are the same for the InAlN/GaN HEMT before and after SA treatment and cannot result in the variation of electron mobility [6]. Figure 24 shows the schematic of the InAlN/GaN HEMT before and after SA surface treatment. The H^+ in SA could easily diffuse through the oxide layer while the larger TFSI molecule cannot. This will protect the InAs surface from becoming contaminated with larger TFSI molecule. Due to the converse piezoelectric effect, the positive charge of H^+ will decrease the polarization charges of the InAlN barrier under the access region, resulting in the decrease of the PCF scattering.



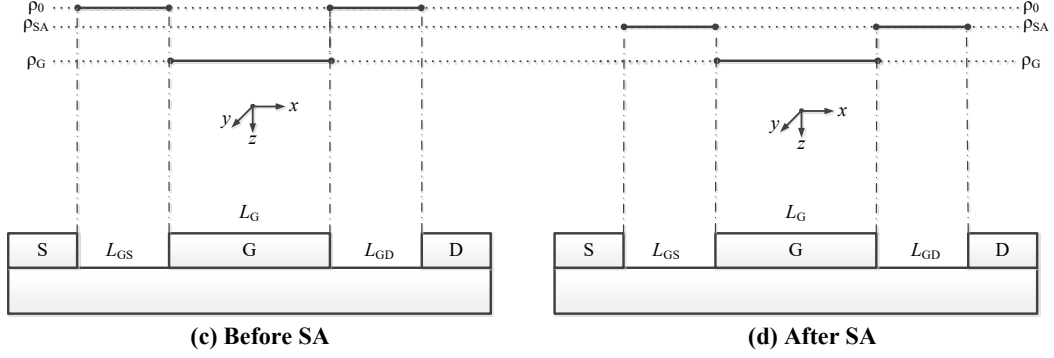


Fig. 24. (a) and (b) Schematic of the InAlN/GaN HEMT before and after SA treatment; (c) and (d) Schematics of the polarization charge distribution of the InAlN barrier before and after SA treatment.

Because of the gate bias, the uniform distribution of the polarization charges at InAlN/GaN interface is broken, as shown in Fig. 24(c), which leads to the PCF scattering generation. Before device processing, the polarization charge density ρ_0 , can be calculated by self-consistently solving Schrodinger's and Poisson's equations. Owing to the converse piezoelectric effect, the polarization charges under the gate region is changed to ρ_G , resulting in the additional polarization charges $\Delta\sigma = \rho_G - \rho_0$. After SA treatment, the polarization charges under the access region is changed to ρ_{SA} (shown in Fig.24(d)), leading to $\Delta\sigma_{SA} = \rho_G - \rho_{SA}$. It is observed that $\Delta\sigma_{SA}$ is much smaller than $\Delta\sigma$. It means the PCF scattering decreases after SA treatment. The PCF scattering potential originating from the additional polarization charges can be written as

$$V(x, y, z) = -\frac{e}{4\pi\epsilon_s\epsilon_0} \int_{-\frac{L_G}{2}}^{\frac{L_G}{2}} dx' \int_0^W \frac{\Delta\sigma}{\sqrt{(x-x')^2 + (y-y')^2 + z^2}} dy'$$

It is known that the two-dimensional channel electrons in InAlN/GaN HEMTs are characterized by a plane wave parallel to the InAlN/GaN interface and a quantized wave perpendicular to the interface, and can be written as $\Psi(x,y,z) = A^{-1/2} \psi(z) \exp(ik_x x + ik_y y)$, where A is the two-dimensional normalization constant that converts the scattering rate per area, k_x , k_y are the components of k in the x -direction and y -direction, respectively. $\psi(z) = (b^3 z^2 / 2)^{1/2} \exp(-bz/2)$ is the Fang-Howard variational wave function and $b = (33m^* e^2 n_{2D} / 8\epsilon_0 \epsilon_s \hbar^2)$ is the variational parameter. Here, m^* is the electron effective mass in GaN, ϵ_0 is the dielectric permittivity, and ϵ_s is the static dielectric constant of GaN. With the obtained wave function $\Psi(x,y,z)$ and the additional scattering potential $V(x,y,z)$, the corresponding matrix element for

the transition from initial state \mathbf{k} to the final state \mathbf{k}' is

$$\begin{aligned} M_{k \rightarrow k'} &= A^{-1} \int_0^\infty \psi_{k'}^*(z) \left[\int_{-\frac{L_G}{2}}^{\frac{L_G}{2}} dx \int_0^W V(x, y, z) \exp(-iq_x x - iq_y y) dy \right] \psi_k(z) dz \\ &= A^{-1} \int_0^\infty \psi_{k'}^*(z) [V(q_x, q_y, z)] \psi_k(z) dz. \end{aligned}$$

Where the middle part of the above equation is the two-dimensional Fourier transform of $V(q_x, q_y, z)$. $q = |2(2m^* \hbar^2 E)^{1/2} \sin(\theta/2)|$ refers to the value change of wave vector for this elastic collisions and q_x, q_y are the components of q in the x -direction and y -direction, respectively. Then the energy dependent scattering rate for the PCF scattering can be written as

$$\frac{1}{\tau_{PCF}(E)} = \frac{Am^*}{2\pi\hbar^3} \int_{-\pi}^{\pi} \left[\frac{M_{k \rightarrow k'}}{S(q, T_e)} \right]^2 (1 - \cos \theta) d\theta.$$

Where θ is the scattering angle between the final state k' and initial state k , and \hbar is the Planck constant. The screening function $S(q, T_e)$ is

$$S(q, T_e) = 1 + \frac{e^2 F(q) \Pi(q, T_e, E)}{2\varepsilon_0 \varepsilon_s q}.$$

Here the form factor, $F(q)$ is

$$F(q) = \int_0^\infty \int_0^\infty \psi^2(z) \psi^2(z') \exp(-q|z - z'|) dz dz',$$

and $\Pi(q, T_e, E)$, the polarizability function, is

$$\Pi(q, T_e, E) = \frac{m^*}{4\pi\hbar^2 k_B T_e} \int_0^\infty \frac{1 - \Theta(q - 2k_F) [1 - (2k_F/q)^2]^{1/2}}{\cosh^2[(E_F - E)/2k_B T_e]} dE.$$

In this equation, $\Theta(x)$ is the usual step function, $k_F = (2\pi n_{2D})^{1/2}$ is the Fermi wave vector, T_e is the electron temperature, E_F is the Fermi energy, and E is the energy.

At the end, numerically calculated energy-dependent scattering time is averaged according to the Fermi statistics, and the momentum relaxation time τ_{PCF} for the PCF scattering can be obtained

$$\tau_{PCF} = \int \tau_{PCF}(E) E \frac{\partial f_0(E)}{\partial E} dE / \int E \frac{\partial f_0(E)}{\partial E} dE.$$

Where the f_0 , the Fermi function, is

$$f_0(E) = \frac{1}{\exp[(E - E_F)/k_B T_e] + 1}.$$

Here k_B is the Boltzmann constant.

In InAlN/GaN HEMTs, the scattering time constant for Polar optical phonon scattering is given by

$$\frac{1}{\tau_{POP}(E)} = \frac{e^2 m^* \hbar \omega_{LO} (\epsilon_h^{-1} - \epsilon_s^{-1}) \epsilon_o^{-1}}{8\pi^2 \hbar^3 [1 - f_0(E)]} \times \int (1 - \cos \theta) \{ [1 - f_0(E + \hbar \omega_{LO})] N_q I(q_{\perp+}) + [1 - f_0(E - \hbar \omega_{LO})] \times \Theta(E - \hbar \omega_{LO}) (N_q + 1) I(q_{\perp-}) \} d\theta.$$

The parameter $\hbar \omega_{LO}$ is the longitudinal optical (LO) phonon energy, ϵ_h is the optical or high frequency dielectric constant of GaN, $q_{\perp+}$ and $q_{\perp-}$ are the scattering wave vectors in the phonon absorption and emission, respectively. The expression for the phonon occupation number, N_q , is given by $N_q = [\exp(\hbar \omega_{LO}/k_B T_e) - 1]^{-1}$. The quantity $I(q_{\perp\pm})$ is defined as $I(q_{\perp\pm}) = \int (q_{\perp\pm}^2 + q_z^2)^{-1} |I(q_z)|^2 dq_z$, where $I(q_z)^2 = b^6 / (b^2 + q_z^2)^3$ for the Fang-Howard wave function.

For acoustic phonon (AP), the analytical formula for the scattering time constant is

$$\frac{1}{\tau_{AP}(E)} = \frac{1}{\tau_{dp}(E)} + \frac{1}{\tau_{pe}(E)} = \frac{3bE_{dp}^2 m^* k_B T_e}{32\pi \hbar^3 C_L} \int \frac{(1 - \cos \theta)}{S^2(q, T_e)} d\theta + \frac{(eh_{14})^2 m^* k_B T_e}{4\pi \hbar^3} \int \frac{(1 - \cos \theta)}{q S^2(q, T_e)} \left[\frac{9}{32C_L} f_L(y) + \frac{13}{32C_T} f_T(y) \right] d\theta.$$

Here E_{dp} is the deformation potential, h_{14} is a piezoelectric tensor element, C_L and C_T are the longitudinal elastic constant and the transverse elastic constant. $f_L(y)$ and $f_T(y)$ refer to the dimensionless form factor for longitudinal and transverse phonon modes, and are given by $f_L(y) = (1 + 6y + 12y^2 + 2y^3)/(1+y)^6$, $f_T(y) = (13 + 78y + 72y^2 + 82y^3 + 36y^4 + 6y^5)/13(1+y)$, respectively, with $y = q/b$.

The scattering time constant due to the interface roughness (IFR) is adopted

$$\frac{1}{\tau_{IFR}(E)} = \frac{m^* (\Delta \lambda)^2}{2\hbar^3} \int \exp\left(-\frac{q^2 \lambda^2}{4}\right) \left[\frac{\Gamma(q)}{S(q, T_e)} \right]^2 (1 - \cos \theta) d\theta.$$

Where Δ is the average displacement of the interface, λ is the auto correlation length of Δ and $\Gamma(q) = e^2 n_{2D} / 2\epsilon_s \epsilon_0$.

The analytical formula for the dislocation scattering (DIS) time constant is

$$\frac{1}{\tau_{DIS}(E)} = \left(\frac{m^* e^4 N_{dis} f^2}{8\pi \epsilon_s^2 \epsilon_0^2 \hbar^3} \right) \int \left\{ \int \psi^*(z) \left[\int \exp(-q|z_i - z| dz_i) \psi(z) dz \right]^2 \frac{1 - \cos \theta}{q^2 S^2(q, T_e)} d\theta \right.$$

Here N_{dis} is the areal dislocation density, c is the lattice constant, and f is the filling factor (assuming completely charged dislocation lines, $f=1$).

Table I. Material parameters used for the calculations.

Parameter	Symbol	Value
Electron effective mass	m^*	$0.22 m_0$
Static dielectric constant	ϵ_s	8.90
High frequency dielectric constant	ϵ_h	5.47
Deformation potential	E_{dp}	8.5 eV
LO-phonon energy	$\hbar\omega_{LO}$	91.2 meV
Piezoelectric constant	h_{14}	0.5 C/m^2
Longitudinal elastic constant	C_L	$2.65 \times 10^{11} \text{ N/m}^2$
Transverse elastic constant	C_T	$4.42 \times 10^{10} \text{ N/m}^2$
Discolation density	N_{dis}	$1 \times 10^{10} \text{ cm}^{-2}$
Lattice constant	c	5.185 \AA
Average displacement of the interface	Δ	1 nm
Auto correlation length of Δ	λ	7.5 nm

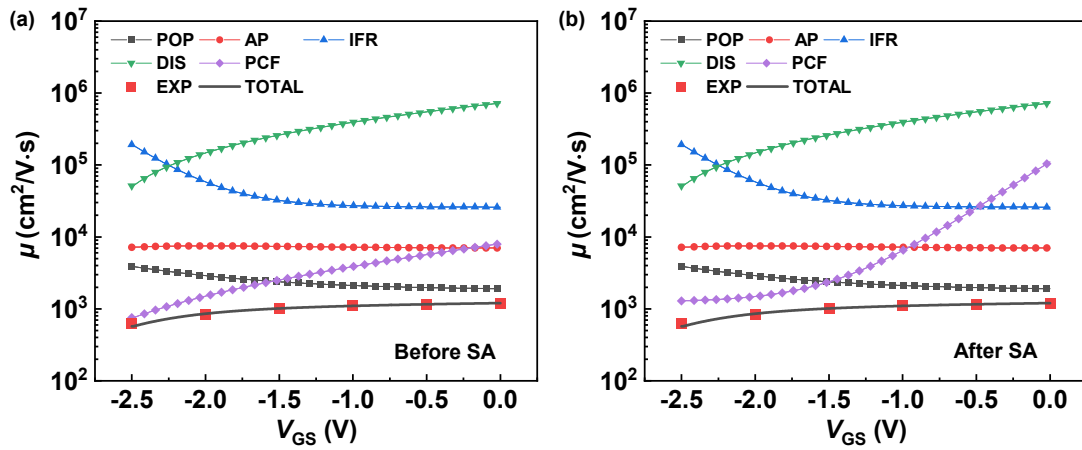


Fig. 25. The calculated specific mobility as a function of forward gate-source voltage for PCF, POP, AP, IFR, and DIS scatterings as well as the total mobility (TOTAL) and the experimental mobility (EXP) at room temperature for the InAlN/GaN before and after SA surface treatment.

The specific parameters in calculation for the average momentum relaxation time τ_{POP} , τ_{AP} , τ_{DIS} and τ_{IFR} are shown in Table I. By $\mu=e\tau/m^*$, the calculated electron mobility values show

good agreement with the experiment values, as shown in **Fig. 25**. POP, AP, DIS, and IFR scattering show the same electron mobility values before and after SA treatment, as discussed above, but the electron mobility limited by PCF scattering is larger for the InAlN/GaN HEMT after SA treatment. These further verify the improved electron mobility of InAlN/GaN HEMT with SA surface treatment.

In summary, superacid treatment on GaN HEMTs enhances the electron mobility due to the reduced PCF scattering. Thus, the device on-current is enhanced. This study provides an efficient way to enhance GaN HEMTs device on-current.

5. Superacid treatment on InAs/MoS₂ heterojunction

Gate tunable rectifying ratio of 2D MoS₂/3D InAs *N-n* type van der Waals (*vdW*) heterojunction is demonstrated. The larger intra conduction band electron tunneling from InAs to MoS₂ than electron injection from MoS₂ to InAs results in rectifying behavior of the *N-n vdW* heterojunction. Under electrostatic gating, the rectifying ratio of the *N-n vdW* heterojunctions can be modulated over 2 orders with a maximum rectifying ratio of $>10^4$. With bis(trifluoronethane) sulfonamide (*TFSI*) treatment on MoS₂ prior to InAs stacking, the modulation of rectifying ratio of the *N-n vdW* heterojunction can be further enhanced with a maximum rectifying ratio of $>10^6$ and *P-MoS₂/n-InAs vdW* heterojunction can be realized under electrostatic gating. The large rectifying ratio and good electrostatic gating of the tunneling current suggest that the 2D MoS₂/3D InAs *N-n vdW* heterojunction is promising for carrier modulation application and a potential candidate for making intra conduction band tunneling field effect transistor (*TFET*).

5.1 InAs/MoS₂ device fabrication

As shown in Fig.26, MoS₂ flakes were grown by chemical vapor deposition (*CVD*) method[24] on a 300-nm SiO₂/Si substrate. InAs ribbons were transferred[25] on the as grown MoS₂ flakes assisted by elastomeric PDMS slab to form InAs/MoS₂ *vdW* heterojunctions. Two sets of InAs/MoS₂ *vdW* heterojunctions were fabricated. For one set of samples, MoS₂ were treated with 0.2 mg/ml bis(trifluoronethane) sulfonamide (*TFSI*) solution at 100°C for 2 min prior to

transfer of InAs ribbons; for the other set of samples, no TFSI treatment was carried out prior to transfer of InAs ribbons. By e-beam lithography and e-beam evaporation, 30-nm Ti/50-nm Au was deposited on MoS₂ and InAs to form source (S) and drain (D) contacts. The samples were then baked at 120°C by oven for 12 h under vacuum to remove moisture and adsorbate on MoS₂ and to reduce contact resistance. Finally, 20-nm ZrO₂ was deposited on sample surface by thermal atomic layer deposition (ALD) assisted with ~1-nm Al₂O₃ as seed layer.

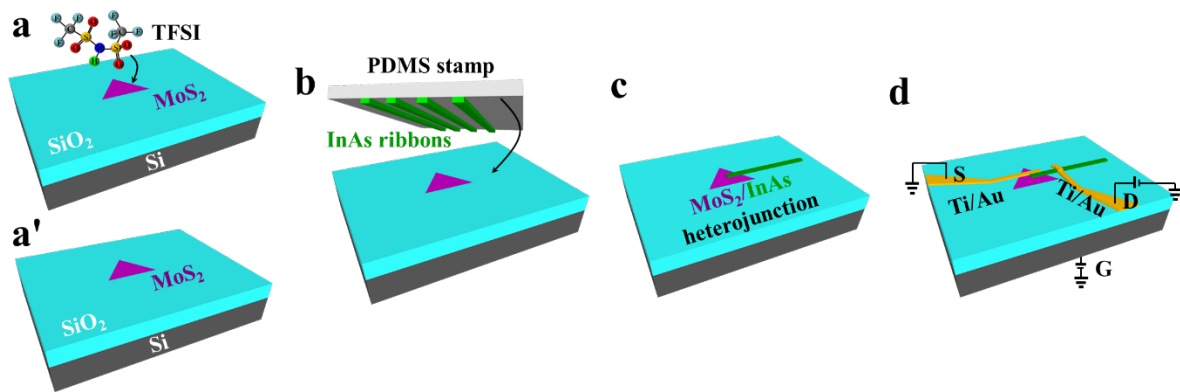


Fig.26 Fabrication process steps of InAs/MoS₂ heterojunction.

5.2 InAs/MoS₂ characterizations

The atomic force microscope (AFM) images were taken by Anasys NanoIR2 system. The Raman spectra were acquired from ThermoScientific DXR Raman microscope. Raman signal is excited by a 532-nm laser with power of 0.1 mW and spot size of 0.7 μm . The exposure time during measurements was 5s. Each measurement was repeated for 5 cycles to improve the signal to noise ratio (SNR). The electrical performance was measured by HP4156B semiconductor parameter analyzer in air ambient at room temperature.

The false-color optical image of fabricated 20-nm InAs/MoS₂ vdW heterojunction is displayed in Figure 27a. Figure 27b displays the cross-section structure of the vdW heterojunction on SiO₂/Si substrate. The thicknesses of MoS₂ flake and InAs ribbon are measured by atomic force microscope (AFM) line scan as shown with green and blue dots in Figure 27c, respectively. The thickness of MoS₂ flake is ~2.6 nm corresponding to a 4L structure [26]; the thickness of InAs is verified as ~20 nm.

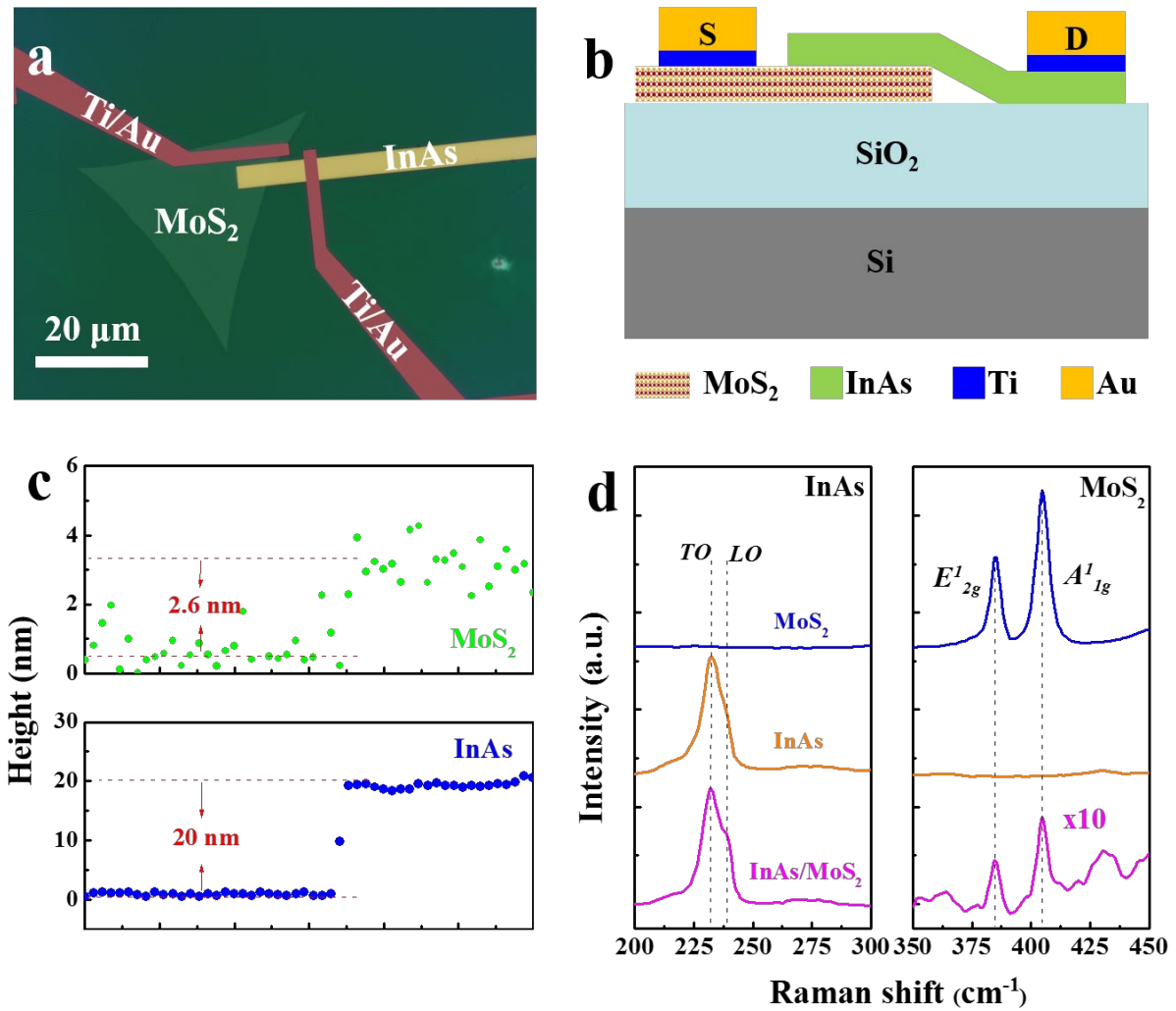


Figure 27. (a) False-color optical image of fabricated 20-nm InAs/MoS₂ *vdW* heterojunction; (b) Cross-section diagram of InAs/MoS₂ *vdW* heterojunction on 300 nm SiO₂/Si substrate; (c) *AFM* line scan for isolated MoS₂ (green dots) and 20-nm InAs (blue dots) on SiO₂; (d) Raman spectra of isolated MoS₂, InAs and InAs/MoS₂ *vdW* heterojunction. InAs and MoS₂ phases at 200~300 cm⁻¹ and 350~450 cm⁻¹, respectively, are used for analysis.

Figure 28a-b show I_{ds} - V_{ds} curves of isolated 20-nm InAs and as grown MoS₂ (without *TFSI* treatment) back-gated *FETs* with gate length of 1 μm, respectively. Absolute values were used for reverse currents to have a better comparison with forward currents. For InAs back-gated *FET*, I_{ds} has a linear dependence on V_{ds} at low V_{ds} under various V_{gs} suggesting formation of InAs/Ti ohmic contact. At larger V_{ds} , as V_{ds} increases, I_{ds} gradually saturates due to pinch-off of InAs channel. Under V_{gs} of -40~40 V, the reverse and forward currents of InAs back-gated *FET* were rather symmetrical. For MoS₂ back-gated *FET*, I_{ds} also has a linear dependence on

V_{ds} under various V_{gs} indicating formation of Ti/MoS₂ ohmic contact. The forward current is slightly higher than the reverse current due to small difference of S and D contact areas and tunneling and thermionic transportation mechanisms between MoS₂ and Ti[27]. Contrary to InAs FET , no pinch-off behavior is observed in MoS₂ FET . These results manifest that no rectifying behavior is obtained in isolated InAs and as grown MoS₂ back-gated $FETs$ under V_{gs} of -40~40 V due to formation of S and D ohmic contacts. The formation of ohmic contact between Ti and InAs is attributed to narrow band gap of InAs (0.35 eV), Fermi level pinning at 0.15 eV above the conduction band minimum (CBM)[28] and small work function of Ti (<4.30 eV)[29]. The observed ohmic contact between multilayer (ML) MoS₂ and Ti agrees well with reported result,[27] which demonstrate a low Schottky barrier height of ~50 meV between ML MoS₂ and Ti. Figure 28c shows the normalized I_{ds} - V_{gs} curves for isolated InAs and as grown MoS₂ back-gated $FETs$ under V_{ds} =100 mV. As V_{gs} decreases from 40 to -40 V, the 20-nm InAs device exhibits an on/off current ratio of $\sim 10^3$. Due to large thickness of back SiO₂ (300 nm), the electrostatic gating of 20-nm InAs device is weak with a subthreshold swing (SS) of ~ 8.8 V/dec. Even though the thickness of MoS₂ is ~ 2.6 nm, the MoS₂ on 300-nm SiO₂/Si cannot be fully depleted with I_{ds} decreasing from 0.5 $\mu A/\mu m$ @40 V to $\sim 0.06 \mu A/\mu m$ @-40 V, suggesting that the MoS₂ flake is heavily n -doped, which is beneficial to achieve Ti/MoS₂ ohmic contact.

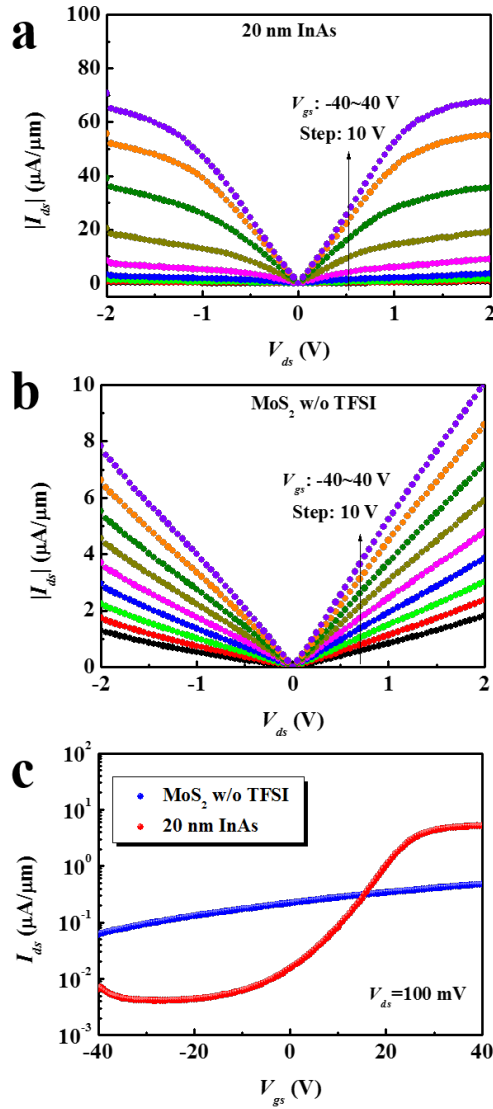


Figure 28. I_{ds} - V_{ds} curves of (a) isolated 20-nm InAs ribbon and (b) 4L MoS₂ on 300-nm SiO₂/Si; (c) Comparison of I_{ds} - V_{gs} curves of isolated 20-nm InAs and 4L MoS₂ on 300-nm SiO₂/Si under $V_{ds}=100$ mV.

By grounding MoS₂ (*S*), the electrical characteristics of InAs/MoS₂ *n-N* type *vdW* heterojunction was measured. Figure 29a displays the I_{ds} - V_{ds} curves of 20-nm InAs/MoS₂ *n-N* type *vdW* heterojunction without *TFSI* treatment of MoS₂ under V_{gs} of -40~40 V. The junction area is $30 \times 4 \mu\text{m}^2$. Absolute value is used for I_{ds} to analyze the rectifying behavior of the *vdW* heterojunctions. As can be seen, both the forward and reverse currents have a dependence on V_{gs} . As V_{gs} increases, both forward and reverse I_{ds} are enhanced indicating electron conduction mechanism in the *n-N* type *vdW* heterojunction. However, the modulation of reverse I_{ds} by V_{gs} is much less effective than that of forward I_{ds} . As $|V_{ds}|$ increases, the reverse I_{ds} increases

exponentially with an ideal factor η of >2.0 suggesting a tunneling-assisted mechanism[30] of reverse I_{ds} ; while the forward current saturates quickly at $V_{ds}<0.5$ V. The device exhibits a tunable rectifying behavior as V_{gs} changes. As mentioned in Figure 28, InAs/Ti and MoS₂/Ti ohmic contacts are formed under various V_{gs} , the tunable rectifying behavior is attributed to the *vdW* heterojunction consequently. Figure 29b shows the dependence of rectifying ratio between reverse and forward I_{ds} at $|V_{ds}|=2$ V on V_{gs} . As V_{gs} increases from -40 to 40 V, the rectifying ratio of 20-nm InAs/MoS₂ *vdW* heterojunction decreases monotonously from 3000 to 16. Figure 29c gives the statistics column of the rectifying ratio modulation range under electrostatic gating for 20-nm InAs/MoS₂ *vdW* heterojunctions from 4 different devices. Overall, by electrostatic gating, the rectifying ratio in 20-nm InAs/MoS₂ *vdW* heterojunctions can be tuned over 2 orders. The maximum rectifying ratio achieved in 20-nm InAs/MoS₂ *vdW* heterojunction is $>10^4$. The results demonstrate that the rectifying ratio of InAs/MoS₂ *vdW* heterojunctions can be effectively tuned by electrostatic gating suggesting effective carrier modulation in 3D InAs and 2D MoS₂ by V_{gs} and V_{ds} .

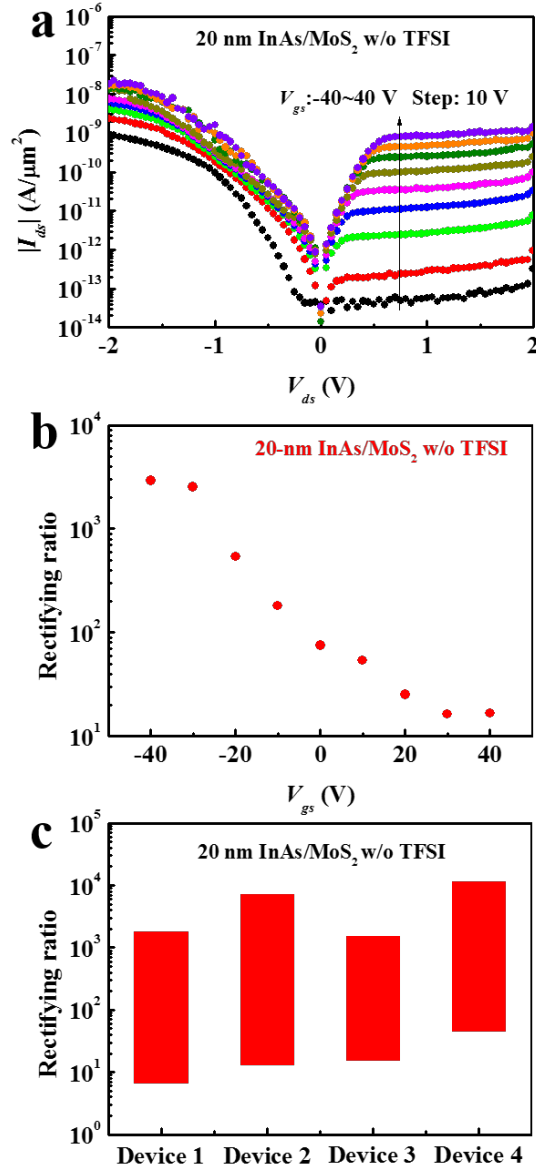


Figure 29. I_{ds} - V_{ds} curves of (a) 20-nm InAs/MoS₂ n - N type vdW heterojunction under V_{gs} of -40~40 V; (b) Dependence of rectifying ratio on V_{gs} for 20-nm InAs/MoS₂ n - N type vdW heterojunction; (c) Statistics column of the rectifying ratio variation range under electrostatic gating in 20-nm InAs/MoS₂ n - N type vdW heterojunction from 4 different devices.

Based on the electrical performance presented above, the band alignment and carrier transportation of InAs/MoS₂ vdW heterojunctions can be qualitatively discussed. From Figure 28c, it is inferred that MoS₂ is heavily n -doped, while InAs is unintentionally slightly n -doped. Figure 30a displays the band diagram of isolated $4L$ MoS₂ and InAs. The electron affinity of $4L$ MoS₂[31] and InAs[32] is 4.0 and 4.9 eV, respectively; the band gap of $4L$ MoS₂[31] and InAs[33] is 1.6 and 0.35 eV, respectively. The InAs/Ti and MoS₂/Ti ohmic contacts do not contribute to the rectifying behavior of vdW heterojunctions, thus are not shown. Since we are

studying n - N type vdW , only the conduction band alignment (CBA) is discussed here. Due to quantum confinement effect (QCE)[25] sublevels are formed in 20-nm InAs. Figure 30b-d shows the CBA of vertical $MoS_2/20\text{-nm InAs}$ vdW heterojunction without gate bias under $V_{ds}=0$ V, $V_{ds}<0$ V and $V_{ds}>0$ V, respectively. The blue solid and blue dash lines at InAs side denote the first sublevel of CB and CBM of 20-nm InAs, respectively. As MoS_2 is in conjunction with InAs, electrons would transfer from wide band gap MoS_2 to narrow band gap InAs resulting in an electric field from MoS_2 to InAs to reach equilibrium condition. The MoS_2 is fully depleted due to the small thickness and the electrons in InAs are confined near the $MoS_2/InAs$ interface due to lower electric potential energy at $MoS_2/InAs$ interface (Figure 30b). Under $V_{ds}>0$ V, the barrier in MoS_2 becomes lower and the electric field is reduced by V_{ds} leading to electron transportation from MoS_2 to InAs (forward I_{ds}). Due to pinch-off of the lateral n -InAs region (as demonstrated in Figure 28a), the forward I_{ds} saturates quickly as forward V_{ds} increases. Under $V_{ds}<0$ V, the electric field is enhanced and the triangle barrier in MoS_2 becomes thinner rendering electron tunneling from InAs to MoS_2 (reverse I_{ds}) assisted by trap states in the gap[34], which is confirmed by the large ideal factor (>2) in I_{ds} - V_{ds} curves of InAs/ MoS_2 vdW heterojunctions (Figure 29a). Since no pinch-off behavior is detected in lateral n - MoS_2 region (as demonstrated in Figure 28b), the reverse I_{ds} increases continuously as $|V_{ds}|$ increases.

It is recalled that the forward I_{ds} , which originates from electron injection from MoS_2 to InAs, can be greatly modulated by V_{gs} . The result suggests that the electrons in MoS_2 can be easily modulated by V_{gs} after charge transfer from MoS_2 to InAs. Figure 30e and 30h display the CBA of vertical $MoS_2/InAs$ vdW heterojunction under $V_{gs}>0$ and $V_{gs}<0$ at $V_{ds}=0$, respectively. The barrier height in MoS_2 under $V_{gs}>0$ and $V_{gs}<0$ increases and decreases, respectively, due to stronger electrostatic gating of MoS_2 compared to that of the upper InAs ribbon. Figure 30f and 30i present the CBA of vertical $MoS_2/InAs$ vdW heterojunction under $V_{gs}>0$ and $V_{gs}<0$ at $V_{ds}>0$, respectively. Under $V_{ds}>0$, the modulation of forward I_{ds} of InAs/ MoS_2 vdW heterojunction by V_{gs} is enhanced compared to that of isolated MoS_2 . Although the electron concentration in InAs of InAs/ MoS_2 vdW heterojunction becomes higher compared to that of isolated InAs, the electron concentration in InAs can be still modulated by V_{gs} since the electrons in InAs are mainly confined at $MoS_2/InAs$ interface. Figure 30g and 30j show the

CBA of vertical MoS₂/InAs *vdW* heterojunction under $V_{gs}>0$ and $V_{gs}<0$ at $V_{ds}<0$, respectively. Under $V_{gs}>0$ and $V_{gs}<0$, the electrons in InAs at MoS₂/InAs interface increases and decreases, respectively, leading to higher and lower reverse I_{ds} (electron tunneling from InAs to MoS₂).

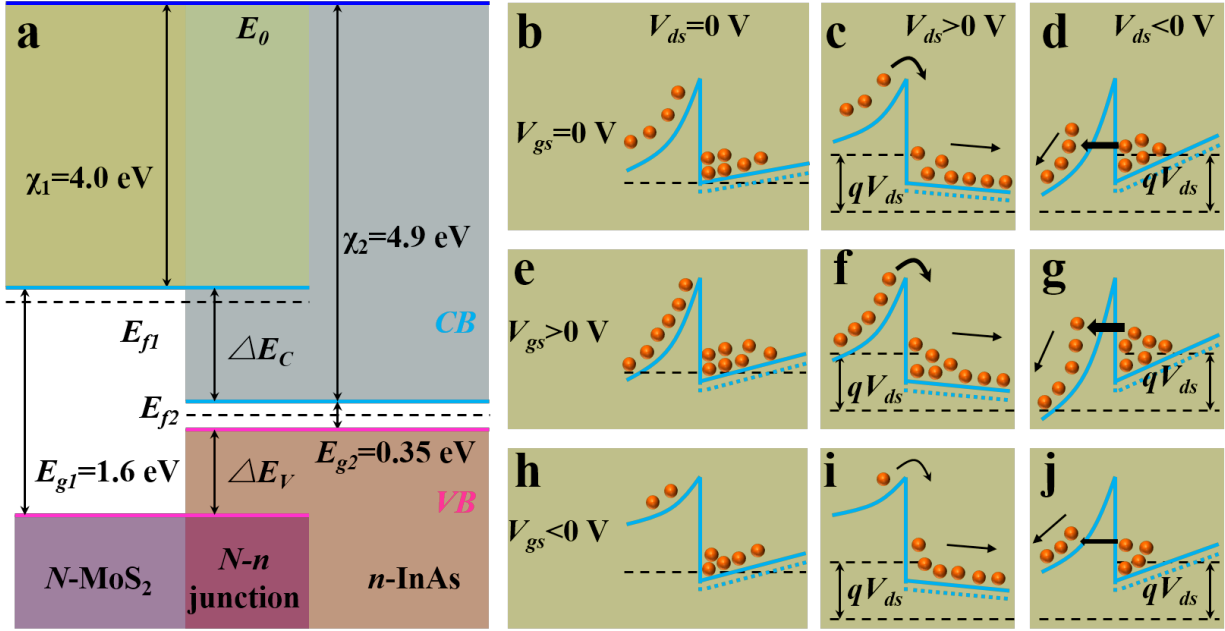


Figure 30. (a) Band structure of isolated MoS₂ and InAs; *CBA* of MoS₂/InAs *vdW* heterojunction under (b) $V_{ds}=0$ V, (c) $V_{ds}>0$ V and (d) $V_{ds}<0$ V at $V_{gs}=0$ V; *CBA* of MoS₂/InAs *vdW* heterojunction under (e) $V_{ds}=0$ V, (f) $V_{ds}>0$ V and (g) $V_{ds}<0$ V at $V_{gs}>0$ V; *CBA* of MoS₂/InAs *vdW* heterojunction under (h) $V_{ds}=0$ V, (i) $V_{ds}>0$ V and (j) $V_{ds}<0$ V at $V_{gs}<0$ V. The blue dash line indicates the *CBM* of InAs.

It has been reported that S vacancies, which provide electrons in MoS₂ and result in unintentionally *n*-type doping of as grown MoS₂ flakes[35] can be effectively passivated after *TFSI* treatment[3, 36]. Figure 31a-b display the I_{ds} - V_{ds} curves of MoS₂ back-gated *FETs* without and with *TFSI* treatment with gate length of 1 μm , respectively. As can be seen, I_{ds} can be modulated over a larger range with *TFSI* treatment compared to that without *TFSI* treatment. Figure 31c compares the I_{ds} - V_{gs} curves of MoS₂ back-gated *FETs* without and with *TFSI* treatment in semi-log and linear scales. A positive shift of threshold voltage is observed for MoS₂ *FET* with *TFSI* treatment compared to that without *TFSI* treatment. Additionally, with *TFSI* treatment, the MoS₂ flake can be fully depleted with an ambipolar transportation

behavior; while without *TFSI* treatment, the MoS₂ flake can be only partially depleted. The positive shift of threshold voltage and enhanced electrostatic gating of MoS₂ flake after *TFSI* treatment can be explained by passivation of S vacancies. The passivation of S vacancies results in less unintentionally *n*-doping of MoS₂ flakes, effectively lowering the doping level in MoS₂ thus rendering positive shift of threshold voltage and the enhanced electrostatic gating of MoS₂. The observation of ambipolar transport in MoS₂ *FET* with *TFSI* treatment has been rarely reported and need to be further studied in future.

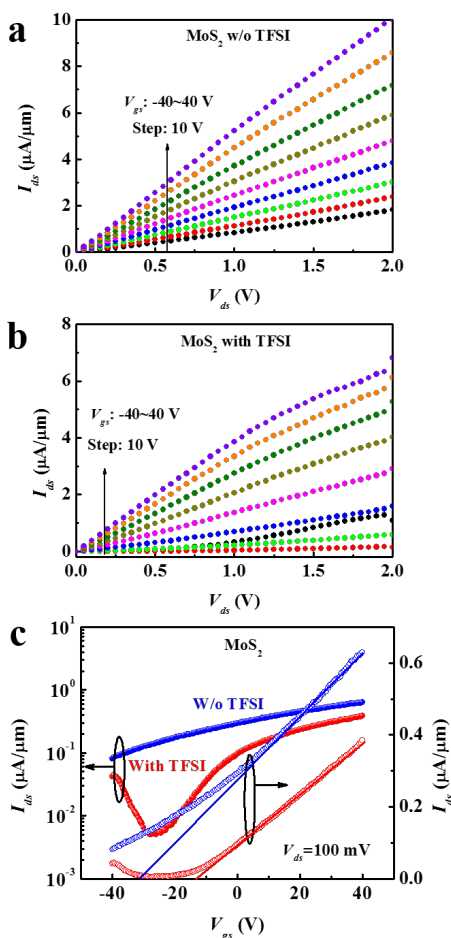


Figure 31. I_{ds} - V_{ds} curves of MoS₂ back-gated *FETs* (a) without and (b) with *TFSI* treatment; (c) Comparison of I_{ds} - V_{gs} curves of MoS₂ back-gated *FETs* without and with *TFSI* treatment in semi-log and linear scales.

Figure 32a shows the I_{ds} - V_{ds} curves for 20-nm InAs/MoS₂ *vdW* heterojunction with *TFSI* treatment. The junction area is $7.7 \times 4 \mu\text{m}^2$. Absolute value is used for I_{ds} . The dependence of reverse I_{ds} (electron tunneling from InAs to MoS₂) on V_{gs} and V_{ds} is similar to that in Figure 29a. Under $V_{gs} > -20$ V, as V_{gs} decreases, the forward I_{ds} (electron transport from MoS₂ to InAs)

decreases monotonously due to electron depletion in MoS₂. A minimum forward I_{ds} is achieved at $V_{gs} \approx -30$ V. Under larger negative V_{gs} , the forward I_{ds} becomes larger with a reverse current direction corresponding to the ambipolar transportation behavior of MoS₂. A P -MoS₂/ n -InAs vdW heterojunction is formed in this case. Figure 32b shows the dependence of rectifying ratio between reverse and forward I_{ds} at $|V_{ds}|=2$ V on V_{gs} . A maximum rectifying ratio is obtained under $V_{gs}=-30$ V. At larger and smaller V_{gs} , the rectifying behavior originates from N - n and P - n junctions, respectively. For the N - n junction, as V_{gs} increases, the rectifying ratio decreases monotonously from 5×10^5 @ $V_{gs}=-30$ V to ~ 100 @ $V_{gs}=40$ V, similar to that without $TFSI$ treatment, but with larger modulation range and larger maximum rectifying ratio. Figure 32c summarized the statistics column of the rectifying ratio variation range under electrostatic gating in 20-nm InAs/MoS₂ vdW heterojunction from 4 different devices. Due to the enhanced electrostatic gating of MoS₂, the maximum rectifying ratio of InAs/MoS₂ vdW heterojunctions becomes larger with a larger modulation range of rectifying ratio. The phenomenon becomes more conspicuous in 40-nm InAs/MoS₂ vdW heterojunctions. For the investigated devices, the maximum rectifying ratio in 20-nm InAs/MoS₂ vdW heterojunctions after $TFSI$ treatment is $>10^6$. The results manifest that the modulation of rectifying ratio of InAs/MoS₂ vdW heterojunction can be effectively enhanced with larger maximum rectifying ratio by $TFSI$ treatment of MoS₂ flakes prior to InAs transfer.

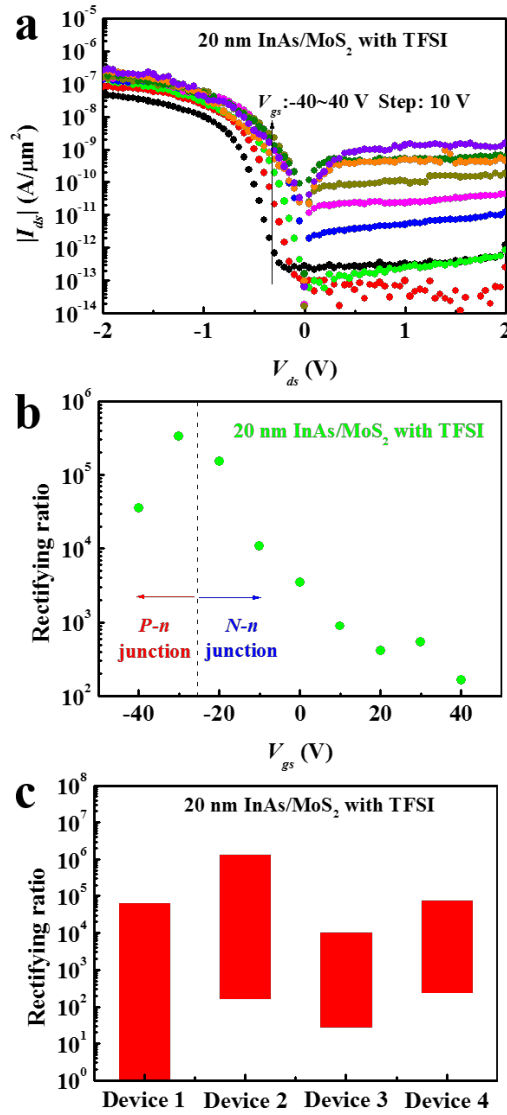


Figure 32. (a) I_{ds} - V_{ds} curves of 20-nm InAs/MoS₂ *vdW* heterojunction with *TFSI* treatment under V_{gs} of -40~40 V. Under $V_{gs} < -20$ V, *P*-MoS₂/*n*-InAs heterojunction was obtained; (b) Dependence of rectifying ratio on V_{gs} for 20-nm InAs/MoS₂ *vdW* heterojunction with *TFSI* treatment. (c) Statistics column of the rectifying ratio variation range under electrostatic gating in 20-nm InAs/MoS₂ *vdW* heterojunction from 4 different devices.

From the above analysis, it is found that the *n*-*N* type InAs/MoS₂ *vdW* heterojunction has higher reverse I_{ds} than forward I_{ds} . Since the reverse I_{ds} originates from intra conduction band electron tunneling from InAs to MoS₂, the results suggest that the *n*-*N* type InAs/MoS₂ *vdW* heterojunction has a great potential for tunneling *FET* (*TFET*). Figure 33a-b displays the I_{ds} - V_{gs} curves of 20-nm InAs/MoS₂ and 40-nm InAs/MoS₂ *n*-*N* type *vdW* heterojunctions with *TFSI* treatment under different forward and reverse V_{ds} , respectively. As $|V_{ds}|$ increases, the difference between forward and reverse I_{ds} becomes larger suggesting smaller *SS* for reverse

I_{ds} than that of forward I_{ds} . The maximum difference between forward and reverse I_{ds} is achieved under $V_{gs} < -20$ V, corresponding to achievement of maximum rectifying ratio. Figure 33c summarizes the dependence of minimum SS on V_{ds} for isolated MoS₂ with *TFSI* treatment, isolated 20-nm InAs and InAs/MoS₂ *vdW* heterojunctions with *TFSI* treatment. The minimum SS is extracted with 1 order variation of I_{ds} . For isolated MoS₂ with *TFSI* treatment and InAs, the minimum SS is around 17 and 9 V/dec, respectively, and increases slightly as V_{ds} increases due to additional modulation effect from V_{ds} . Impressively, for the reverse I_{ds} (tunneling current) of 20-nm InAs/MoS₂ and 40-nm InAs/MoS₂ *vdW* heterojunctions, the minimum SS is much smaller than that of isolated MoS₂ and InAs. As reverse V_{ds} increases, the minimum SS of the tunneling current for 20-nm InAs/MoS₂ *vdW* heterojunction decreases from 6 V/dec @ $V_{ds}=0.05$ V to 3.6 V/dec @ $V_{ds}=0.25$ V; the minimum SS of the tunneling current for 40-nm InAs/MoS₂ *vdW* heterojunction decreases from 5.0 V/dec @ $V_{ds}=0.25$ V to 2.1 V/dec @ $V_{ds}=1.0$ V. The decreases of minimum SS under larger reverse V_{ds} for the tunneling current is due to narrower triangular barrier between InAs and MoS₂ effectively increasing the tunneling current. The SS can be theoretically expressed as:[37]

$$SS = \frac{\partial V_{gs}}{\partial \psi_s} \frac{\partial \psi_s}{\partial (\log_{10} I_{ds})} = \left(1 + \frac{C_d}{C_{ox}} \right) \frac{kT}{q} \ln 10, (1)$$

where Ψ_s is surface potential, kT/q is the thermal voltage, C_d and C_{ox} are the depletion and oxide capacitance, respectively. By scaling down the dielectric to an 8-nm ZrO₂ (dielectric constant: ~20), the SS of potential *TFET* could be predicted by equation (1). Figure 32d displays the predicted SS for the devices discussed above. It is found that the SS of tunneling current for InAs/MoS₂ *TFET* would be much lower than that of isolated InAs and MoS₂ *FETs* with achievable SS of <70 mV/dec. Through improving the *n*-type doping concentration of MoS₂, higher tunneling current can be expected since the barrier width in MoS₂ would be reduced. As the thickness of MoS₂ reduces from few layers to monolayer, the electron affinity of MoS₂ would increase[31]. The barrier width of MoS₂ in monolayer MoS₂/InAs is expected to be larger than that in *4L* MoS₂/InAs *vdW* heterojunction, leading to a more dependent of I_{ds} on V_{gs} . Thus, a smaller SS can be expected for the tunneling current of monolayer MoS₂/InAs *vdW*

heterojunctions. The results suggest that the 2D MoS₂/3D InAs *n-n* vdW heterojunctions have a great potential for *TFET* with intra conduction band tunneling mechanism.

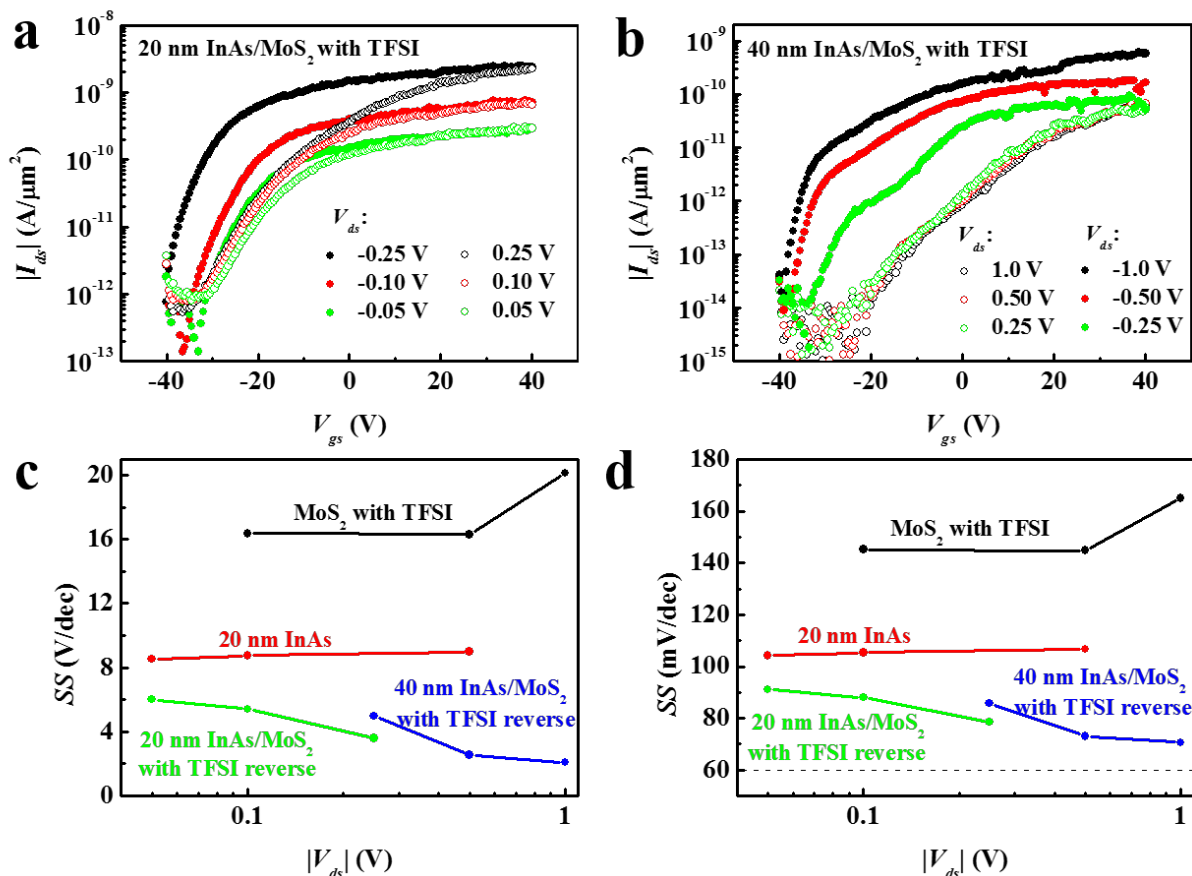


Figure 32. (a) I_{ds} - V_{gs} curves of 20-nm InAs/MoS₂ vdW heterojunction with *TFSI* treatment under $|V_{ds}|=0.05$, 0.10 and 0.25 V; (b) I_{ds} - V_{gs} curves of 40-nm InAs/MoS₂ vdW heterojunction with *TFSI* treatment under $|V_{ds}|=0.25$, 0.50 and 1.0 V; (c) Dependence of minimum SS on V_{ds} for isolated MoS₂ with *TFSI* treatment, isolated 20-nm InAs, 20-nm InAs/MoS₂ and 40-nm InAs/MoS₂ vdW heterojunctions with *TFSI* treatment; (d) Predicted dependence of minimum SS on V_{ds} for isolated MoS₂ with *TFSI* treatment, isolated 20-nm InAs, 20-nm InAs/MoS₂ and 40-nm InAs/MoS₂ vdW heterojunctions with *TFSI* treatment on 8-nm ZrO₂ back gate oxide.

In summary, 2D MoS₂/3D InAs *n-n* type vdW heterojunctions with gate tunable rectifying ratio are demonstrated. The larger intra conduction band electron tunneling from InAs to MoS₂ under reverse V_{ds} (MoS₂ as source) than electron injection from MoS₂ to InAs under forward V_{ds} results in rectifying behavior of the *n-n* vdW heterojunction. Under electrostatic gating, the rectifying ratio of the *n-n* vdW heterojunctions can be effectively tuned over 2 orders with a maximum rectifying ratio of $>10^4$. Through *TFSI* treatment on MoS₂ prior to InAs stacking, the modulation of rectifying ratio of the *n-n* vdW heterojunction can be further enhanced with

a maximum rectifying ratio of $>10^6$ and *p*-MoS₂/*n*-InAs *vdW* heterojunction can be realized under electrostatic gating. The large rectifying ratio and good electrostatic gating of the tunneling current suggest that the 2D MoS₂/3D InAs *n-n* *vdW* heterojunctions is promising for carrier modulation application and a potential candidate for making *TFET*.

Conclusions

We have successfully enhanced device performances by SA treatment on different devices and investigated their respective effects. **On MoS₂ devices**, that water desorbs from MoS₂ after TFSI treatment and it can effectively reduce the SS. It may be a general strategy to improve or recover the electrical performance of other S-containing 2D TMDs. **On InAs devices**, it was found that the interfacial oxide at the InAs/ZrO₂ interface was effectively reduced after TFSI treatment due to strong protonating nature of SA solution. **On TiO₂ devices**, SA treatment is shown as effective method to enhance the current drivability of TiO₂ TFTs by ionic doping of the offset region. For future study, we will continue to apply it on other semiconductor/oxide interfaces to explore more mechanisms and extend its THz applications. **On GaN HEMTs**, channel mobility is enhanced due to reduced PCF. **On InAs/MoS₂ heterojunction**, through *TFSI* treatment on MoS₂ prior to InAs stacking, the modulation of rectifying ratio of the *n-n* *vdW* heterojunction can be further enhanced with a maximum rectifying ratio of $>10^6$.

SF425 and DD882 forms are submitted by research office separately.

References

- [1]S. N. Suarez, J. R. P. Jayakody, S. G. Greenbaum, T. Zawodzinski, and J. J. Fontanella, "A Fundamental Study of the Transport Properties of Aqueous Superacid Solutions," *J. Phys. Chem. B*, vol. 114, pp. 8941-8947, 2010/07/15 2010.
- [2]H. Kim, D.-H. Lien, M. Amani, J. W. Ager, and A. Javey, "Highly Stable Near-Unity Photoluminescence Yield in Monolayer MoS₂ by Fluoropolymer Encapsulation and Superacid Treatment," *ACS Nano*, vol. 11, pp. 5179-5185, 2017/05/23 2017.
- [3]D.-H. Lien, S. Z. Uddin, M. Yeh, M. Amani, H. Kim, J. W. Ager, E. Yablonovitch, and A. Javey, "Electrical suppression of all nonradiative recombination pathways in monolayer semiconductors," *Science*, vol. 364, p. 468, 2019.
- [4]M. Amani, D.-H. Lien, D. Kiriya, J. Xiao, A. Azcatl, J. Noh, S. R. Madhvapathy, R. Addou, S. Kc, M. Dubey, K. Cho, R. M. Wallace, S.-C. Lee, J.-H. He, J. W. Ager, X. Zhang, E. Yablonovitch, and A. Javey, "Near-unity photoluminescence quantum yield in MoS₂," *Science*, vol. 350, p. 1065, 2015.
- [5]G. H. Han, N. J. Kybert, C. H. Naylor, B. S. Lee, J. Ping, J. H. Park, J. Kang, S. Y. Lee, Y. H. Lee, R. Agarwal, and A. T. C. Johnson, "Seeded growth of highly crystalline molybdenum disulphide monolayers at controlled locations," *Nature Communications*, vol. 6, p. 6128, 2015/01/28 2015.
- [6]H. H. Berger, "Models for contacts to planar devices," *Solid-State Electron.*, vol. 15, pp. 145-158, 1972/02/01/ 1972.
- [7]S. Mignuzzi, A. J. Pollard, N. Bonini, B. Brennan, I. S. Gilmore, M. A. Pimenta, D. Richards, and D. Roy, "Effect of disorder on Raman scattering of single-layer MoS_2 ," *Phys. Rev. B*, vol. 91, p. 195411, 05/11/ 2015.
- [8]S. Bertolazzi, S. Bonacchi, G. Nan, A. Pershin, D. Beljonne, and P. Samorì, "Engineering Chemically Active Defects in Monolayer MoS₂ Transistors via Ion-Beam Irradiation and Their Healing via Vapor Deposition of Alkanethiols," *Adv. Mater.*, vol. 29, p. 1606760, 2017/05/01 2017.
- [9]B. H. Kim, M. Park, M. Lee, S. J. Baek, H. Y. Jeong, M. Choi, S. J. Chang, W. G. Hong, T. K. Kim, H. R. Moon, Y. W. Park, N. Park, and Y. Jun, "Effect of sulphur vacancy on geometric and electronic structure of MoS₂ induced by molecular hydrogen treatment at room

temperature," *RSC Adv.*, vol. 3, pp. 18424-18429, 2013.

[10]C. M. Lee, C. H. Jin, C. H. Ahn, H. K. Cho, J. H. Lim, S. M. Hwang, and J. Joo, "Enhanced Gas Sensing Performance of Hydrothermal MoS₂ Nanosheets by Post-Annealing in Hydrogen Ambient," *Bull. Chem. Soc. Jpn.*, vol. 92, pp. 1094-1099, 2019/06/15 2019.

[11]S. Andleeb, A. Kumar Singh, and J. Eom, "Chemical doping of MoS₂ multilayer by p-toluene sulfonic acid," *Sci. Technol. Adv. Mater.*, vol. 16, p. 035009, 2015/06/20 2015.

[12]Y. Zeng, S. Khandelwal, K. F. Shariar, Z. Wang, G. Lin, Q. Cheng, P. Cui, R. Opila, G. Balakrishnan, S. Addamane, P. Taheri, D. Kiriya, M. Hettick, and A. Javey, "InAs FinFETs Performance Enhancement by Superacid Surface Treatment," *IEEE Trans. Electron Devices*, vol. 66, pp. 1856-1861, 2019.

[13]H. Lu, A. Kummel, and J. Robertson, "Passivating the sulfur vacancy in monolayer MoS₂," *APL Mater.*, vol. 6, p. 066104, 2018/06/01 2018.

[14]E. Paparazzo, "XPS and auger spectroscopy studies on mixtures of the oxides SiO₂, Al₂O₃, Fe₂O₃ and Cr₂O₃," *J. Electron Spectrosc. Relat. Phenom.*, vol. 43, pp. 97-112, 1987/01/01/ 1987.

[15]S. Yamamoto, H. Bluhm, K. Andersson, G. Ketteler, H. Ogasawara, M. Salmeron, and A. Nilsson, "In situ x-ray photoelectron spectroscopy studies of water on metals and oxides at ambient conditions," *J. Phys.: Condens. Matter*, vol. 20, p. 184025, 2008/04/17 2008.

[16]H. Ko, K. Takei, R. Kapadia, S. Chuang, H. Fang, P. W. Leu, K. Ganapathi, E. Plis, H. S. Kim, S.-Y. Chen, M. Madsen, A. C. Ford, Y.-L. Chueh, S. Krishna, S. Salahuddin, and A. Javey, "Ultrathin compound semiconductor on insulator layers for high-performance nanoscale transistors," *Nature*, vol. 468, pp. 286-289, 2010/11/01 2010.

[17]K. Takei, R. Kapadia, H. Fang, E. Plis, S. Krishna, and A. Javey, "High quality interfaces of InAs-on-insulator field-effect transistors with ZrO₂ gate dielectrics," *Applied Physics Letters*, vol. 102, p. 153513, 2013/04/15 2013.

[18]S. Khandelwal, J. P. Duarte, A. Medury, Y. S. Chauhan, and C. Hu, "New industry standard FinFET compact model for future technology nodes," in *2015 Symposium on VLSI Technology (VLSI Technology)*, 2015, pp. T62-T63.

[19]T. Tsuchiya, K. Terabe, and M. Aono, "All-solid-state electric-double-layer transistor based on oxide ion migration in Gd-doped CeO₂ on SrTiO₃ single crystal," *Applied Physics Letters*,

vol. 103, p. 073110, 2013.

[20]J. Zhang, M. G. Sales, G. Lin, P. Cui, P. Pepin, J. M. Vohs, S. McDonnell, and Y. Zeng, "Ultrathin-Body TiO₂ Thin Film Transistors With Record On-Current Density, ON/OFF Current Ratio, and Subthreshold Swing via O₂ Annealing," *IEEE Electron Device Letters*, vol. 40, pp. 1463-1466, 2019.

[21]S. Fathipour, P. Pandey, S. Fullerton-Shirey, and A. Seabaugh, "Electric-double-layer doping of WSe₂ field-effect transistors using polyethylene-oxide cesium perchlorate," *Journal of Applied Physics*, vol. 120, p. 234902, 2016.

[22]M. Amani, D.-H. Lien, D. Kiriya, J. Xiao, A. Azcatl, J. Noh, S. R. Madhvapathy, R. Addou, K. Santosh, and M. Dubey, "Near-unity photoluminescence quantum yield in MoS₂," *Science*, vol. 350, pp. 1065-1068, 2015.

[23]A. Elbourne, S. McDonald, K. Voichovsky, F. Endres, G. G. Warr, and R. Atkin, "Nanostructure of the ionic liquid–graphite stern layer," *ACS nano*, vol. 9, pp. 7608-7620, 2015.

[24]G. H. Han, N. J. Kybert, C. H. Naylor, B. S. Lee, J. Ping, J. H. Park, J. Kang, S. Y. Lee, Y. H. Lee, R. Agarwal, and A. T. C. Johnson, "Seeded growth of highly crystalline molybdenum disulphide monolayers at controlled locations," *Nat. Commun.*, vol. 6, p. 6128, 01/28/online 2015.

[25]H. Ko, K. Takei, R. Kapadia, S. Chuang, H. Fang, P. W. Leu, K. Ganapathi, E. Plis, H. S. Kim, S.-Y. Chen, M. Madsen, A. C. Ford, Y.-L. Chueh, S. Krishna, S. Salahuddin, and A. Javey, "Ultrathin compound semiconductor on insulator layers for high-performance nanoscale transistors," *Nat.*, vol. 468, p. 286, 11/10/online 2010.

[26]B. Radisavljevic, A. Radenovic, J. Brivio, V. Giacometti, and A. Kis, "Single-layer MoS₂ transistors," *Nature nanotechnology*, vol. 6, pp. 147-150, 2011.

[27]S. Das, H.-Y. Chen, A. V. Penumatcha, and J. Appenzeller, "High Performance Multilayer MoS₂ Transistors with Scandium Contacts," *Nano Lett.*, vol. 13, pp. 100-105, 2013/01/09 2013.

[28]N. Li, E. S. Harmon, J. Hyland, D. B. Salzman, T. P. Ma, Y. Xuan, and P. D. Ye, "Properties of InAs metal-oxide-semiconductor structures with atomic-layer-deposited Al₂O₃ Dielectric," *Appl. Phys. Lett.*, vol. 92, p. 143507, 2008/04/07 2008.

[29]R. G. Wilson, "Vacuum Thermionic Work Functions of Polycrystalline Be, Ti, Cr, Fe, Ni, Cu, Pt, and Type 304 Stainless Steel," *J. Appl. Phys.*, vol. 37, pp. 2261-2267, 1966/05/01 1966.

- [30]K. Mayes, A. Yasan, R. McClintock, D. Shiell, S. R. Darvish, P. Kung, and M. Razeghi, "High-power 280 nm AlGaIn light-emitting diodes based on an asymmetric single-quantum well," *Appl. Phys. Lett.*, vol. 84, pp. 1046-1048, 2004/02/16 2004.
- [31]S. L. Howell, D. Jariwala, C.-C. Wu, K.-S. Chen, V. K. Sangwan, J. Kang, T. J. Marks, M. C. Hersam, and L. J. Lauhon, "Investigation of Band-Offsets at Monolayer–Multilayer MoS₂ Junctions by Scanning Photocurrent Microscopy," *Nano Lett.*, vol. 15, pp. 2278-2284, 2015/04/08 2015.
- [32]G. W. Gobeli and F. G. Allen, "Photoelectric Properties of Cleaved GaAs, GaSb, InAs, and InSb Surfaces; Comparison with Si and Ge," *Phys. Rev.*, vol. 137, pp. A245-A254, 01/04/ 1965.
- [33]Z. M. Fang, K. Y. Ma, D. H. Jaw, R. M. Cohen, and G. B. Stringfellow, "Photoluminescence of InSb, InAs, and InAsSb grown by organometallic vapor phase epitaxy," *J. Appl. Phys.*, vol. 67, pp. 7034-7039, 1990/06/01 1990.
- [34]C.-H. Lee, G.-H. Lee, A. M. van der Zande, W. Chen, Y. Li, M. Han, X. Cui, G. Arefe, C. Nuckolls, T. F. Heinz, J. Guo, J. Hone, and P. Kim, "Atomically thin p–n junctions with van der Waals heterointerfaces," *Nat. Nanotechnol.*, vol. 9, p. 676, 08/10/online 2014.
- [35]Y.-C. Lin, W. Zhang, J.-K. Huang, K.-K. Liu, Y.-H. Lee, C.-T. Liang, C.-W. Chu, and L.-J. Li, "Wafer-scale MoS₂ thin layers prepared by MoO₃ sulfurization," *Nanoscale*, vol. 4, pp. 6637-6641, 2012.
- [36]M. Amani, D.-H. Lien, D. Kiriya, J. Xiao, A. Azcatl, J. Noh, S. R. Madhvapathy, R. Addou, S. Kc, M. Dubey, K. Cho, R. M. Wallace, S.-C. Lee, J.-H. He, J. W. Ager, X. Zhang, E. Yablonovitch, and A. Javey, "Near-unity photoluminescence quantum yield in MoS₂," *Sci.*, vol. 350, p. 1065, 2015.
- [37]S. Salahuddin and S. Datta, "Use of Negative Capacitance to Provide Voltage Amplification for Low Power Nanoscale Devices," *Nano Lett.*, vol. 8, pp. 405-410, 2008/02/01 2008.